Containerless Processing of Stainless Steel

by

Quoc Cuong Bui

Submitted to the Department of Materials Science and Engineering
in partial fulfillment of the requirements for the degree of

Master of Science in Materials Science and Engineering

at the

MASSACHUSETTS INSTITUTE OF TECHNOLOGY

June 1998

Author .....
Department of Materials Science and Engineering
May 8, 1998

Certified by .....
Merton C. Flemings
Toyota Professor of Materials Processing
Thesis Supervisor

Accepted by .....
Linn W. Hobbs
John F. Elliott Professor of Materials
Chairman, Department Committee on Graduate Students

Containerless Processing of Stainless Steel

by

Quoc Cuong Bui

Submitted to the Department of Materials Science and Engineering
on May 8, 1998, in partial fulfillment of the
requirements for the degree of
Master of Science in Materials Science and Engineering

Abstract

The rapid solidification of a Fe-12 wt% Cr-16 wt% Ni alloy in containerless processing conditions was investigated using an electromagnetic levitation facility. High-speed video and pyrometry allowed the study of phase selection and secondary nucleation mechanisms for that alloy as well as measurements of delay times and growth velocities.

Double recalescence events were observed for the first time at temperatures near the T_0 temperature of the metastable ferritic phase, defining a value of the critical undercooling for metastable bcc nucleation significantly lower than previously reported. Phase selection during recalescence was successfully performed by use of different trigger materials: at temperatures below the bcc T_0, a bcc Fe trigger induced the primary nucleation of the metastable bcc phase which subsequently transformed into the stable fcc phase while an fcc Ni trigger caused the nucleation of the equilibrium fcc phase.

Growth velocities were characterized for the δ phase growing into the undercooled liquid, the γ phase growing into the undercooled liquid and the γ phase growing into the semi-solid primary bcc. It was found that a critical undercooling exists at which the growth velocity of the primary ferritic phase is equal to that of the secondary austenitic phase into the primary semi-solid. At undercoolings below this critical value, the equilibrium γ can overwhelm the primary δ and break into the undercooled liquid. Such a double recalescence event can therefore appear as a single event depending on the geometry of the detection equipment. From this observation, a model based on velocity and delay time arguments was proposed to explain discrepancies with earlier works.

Thesis Supervisor: Merton C. Flemings
Title: Toyota Professor of Materials Processing

Acknowledgments

I would like to express my gratitude to Professor Flemings who gave me the opportunity to work on such a challenging project and provided me with helpful guidance throughout the course of my research. Special thanks go to Dr. Douglas Matson and John Lum for their invaluable help and support, particularly for the velocity model routines. I also want to thank Xinyu Zhao for his assistance on pyrometry, Dr. Toshihiko Koseki and Nippon Steel for providing the alloy, NASA who funded this project under contract NAG8-1230 and lastly, all the members of the MIT Solidification Group.

This work is dedicated to my family, both in France and in the United States who, despite the distance, supported me unconditionally and to my dear friend Tien who made the lonely french dude that I am feel more at home.

Contents

List of Figures

List of Tables

Chapter 1

Introduction

The study of phase selection between the equilibrium austenitic phase and the metastable ferritic phase during the rapid solidification of stainless steel finds direct application in the commercially-important process of strip casting. A considerable amount of research has been done in this area. Complex stainless steel alloys have been simulated with model Fe-Cr-Ni ternary alloys to define the phase selection and undercooling behaviors during rapid solidification. Due to the reactive nature of molten metallic solutions containing Chromium, ground-based electromagnetic levitation processing techniques have been successfully used in order to obtain the liquid phase in the metastable undercooled condition.

Using a containerless processing technique and rapid quenching, Koseki and Flemings presented evidence of the formation of the metastable body-centered-cubic phase prior to conversion to the stable face-centered-cubic phase during the solidification of undercooled Fe-Cr-Ni alloys, thus providing a physical explanation for the "double recalescence phenomenon" observed in a variety of systems [1, 2, 3, 4].

Volkmann *et al.* [5, 6] and Moir *et al.* [7] carried out similar studies independently in Germany and reached the same conclusions, that above a certain critical undercooling, the nucleation of the metastable bcc phase occurs first, followed by the nucleation of the stable fcc phase. This critical undercooling is significantly depressed below the T_0 temperature of the metastable phase.

Space experiments conducted by the Solidification Research Group of Professor Flemings at MIT [8, 9] aboard the space shuttle Columbia during NASA mission STS 83, Microgravity Space Laboratory (MSL-1) are in disagreement with the aforementioned ground-

based works. Under these conditions, the critical undercooling was also depressed below the T_0 temperature but double recalescence could be observed when samples were undercooled to just below the solidus of the δ phase.

The purpose of this work is to clarify this controversy and to provide ground-based data on the same flight alloy for a comparison between the behaviors under 1-g and micro-gravity conditions.

Chapter 2

Literature Survey

A thorough study of the solidification of undercooled 70 wt% Fe-Cr-Ni alloys was carried out by Koseki and Flemings over a broad composition range using an electromagnetic levitation technique [1, 2, 3, 4]. They provided pyrometric [2] and metallographic evidences [3] to support the contention that the "double recalescence" phenomenon observed in hypoeutectic alloys (lower Chromium content) below a certain "transition temperature" could be attributed to the formation of the metastable bcc phase shortly followed by the formation of the equilibrium fcc phase. They suggested that the phase selection mechanism was linked to the preferred nucleation of the ferritic phase [2]. It was observed that the transition temperature is significantly depressed below the T_0 temperature of the bcc phase and decreases sharply with decreasing Chromium content [2]. The influence of the undercooling on the delay time (duration between the nucleation of the bcc and the fcc) was indicated [2]. They also reported that the nature of the chill does not induce any difference in phase selection behavior during sample quenching [4].

A similar investigation conducted independently by Volkmann *et al.* [5, 6] confirmed the results and conclusions of Koseki over a broad range of composition selected from the 69 wt% Fe isopleth. High-speed pyrometry allowed observation of the double recalescence in austenitic alloys, corroborated by X-ray phase analysis, and measurements of growth velocities of both δ and γ phases. It was determined that the fcc phase grows faster than the bcc phase for the same undercooling, thus excluding a phase selection mechanism by growth of competing phases. They hypothesized that phase selection was controlled by the preferred nucleation of the ferritic phase [6]. A nucleation model based on the Diffuse

Interface Theory (DIT) was therefore proposed, from which, a theoretical phase selection diagram was derived. It predicts that in hypoeutectic alloys, the critical undercooling necessary for the transition to metastable bcc phase solidification is greater than the gap between the liquidus of the fcc and the T_0 temperature of the bcc [5].

Matson *et al.* investigated the phenomenon of double recalescence using a high-speed video imaging technique on the 15 wt% and 16 wt% Cr alloys of Koseki [10]. Video evidences of the formation of the metastable phase with subsequent formation of the equilibrium phase were presented. The video data permitted the identification of several mechanisms for the secondary nucleation: it was observed that the secondary nucleation site appeared either at the primary location, elsewhere within the semi-solid region or on the edge of the growing bcc phase. Three types of growth velocities were characterized and measured from the digital images: the velocity of the metastable δ phase growing into the undercooled liquid, of the stable γ phase growing into the undercooled liquid and of the stable phase growing into the semi-solid primary bcc phase. Contrary to previous works, the velocity data presented does not support the existence of a depressed transition temperature below the solidus temperature of the metastable phase.

Double recalescence in Fe-Cr-Ni alloys was examined by Moir and Herlach from the prospective of growth velocity measurements based on a high-speed pyrometry technique [7]. They confirmed the slower growth velocity of the bcc phase compared to that of the fcc phase at same composition and undercooling observed by Volkmann *et al.*, as shown in Figure 2-1. The critical transition temperature, determined from velocity data, was compared to nucleation models (Classical Nucleation Theory and DIT). It was found that it always lies far below the bcc T_0 temperature and decreases with decreasing Chromium content, in agreement with the conclusions of Koseki and Volkmann. Furthermore, no effect on phase selection was observed by selection of fcc or bcc trigger material. This same observation was made for binary Fe-Ni alloys by Lum [11].

A recent breakthrough was made during NASA mission STS 83 aboard the Microgravity Science Laboratory on Columbia. Using an electromagnetic levitation and heating technique, a research group from MIT led by Professor Flemings and Dr. Matson investigated the rapid solidification of two 72 wt% Fe-Cr-Ni alloys in micro-gravity [9]. Delay times and velocities were measured using high-speed one-color pyrometry and both spontaneous and triggered nucleation tests were performed. Double recalescence was observed

at much lower undercoolings than previously seen, bringing the transition temperature up to the solidus of the metastable δ phase. This is illustrated in Figure 2-2 which represents a pseudo-binary isopleth at 72 wt% Fe calculated using Thermo-Calc from thermo-physical property data presented in Table 2.1. From this phase diagram, it can be seen that two test conditions bracket the solidus line of the bcc: in one case, a single recalescence event is observed just above the projected solidus for the alloy, in the other, a double recalescence event just below. This is in clear disagreement with earlier ground-based work.

In summary, ground-based results from Koseki, Volkmann and Moir show the existence of a depressed critical undercooling far below the T_0 temperature of the δ phase for the transition to metastable phase nucleation. Both ground-based and space results from Matson disagree with the investigations of the above authors on the extent of the depression: the observed transition temperature corresponds to the bcc solidus. In order to facilitate the comparison of those results, these experiments are summarized in Table 2.2 and the different alloy compositions of those studies are plotted in a ternary diagram in Figure 2-3.

An original experimental set-up was designed for this work. It uses a similar electromagnetic levitation technique as the investigations discussed above but combines high-speed video and high-speed pyrometry data collection. The details are given in the next chapter.

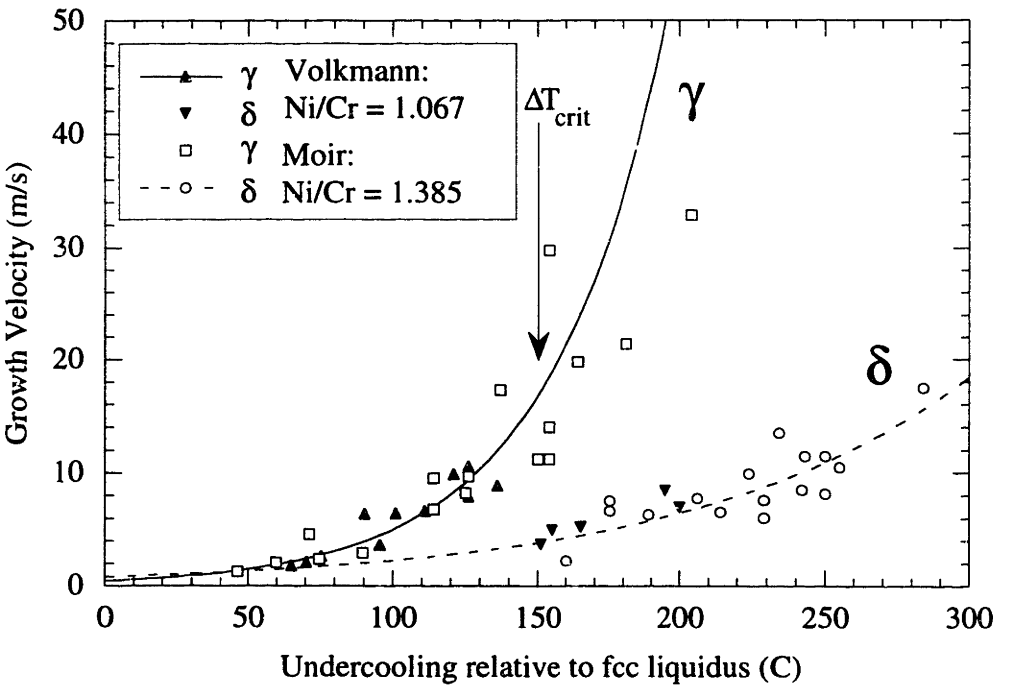

Figure 2-1: Velocity data from Volkmann and Moir

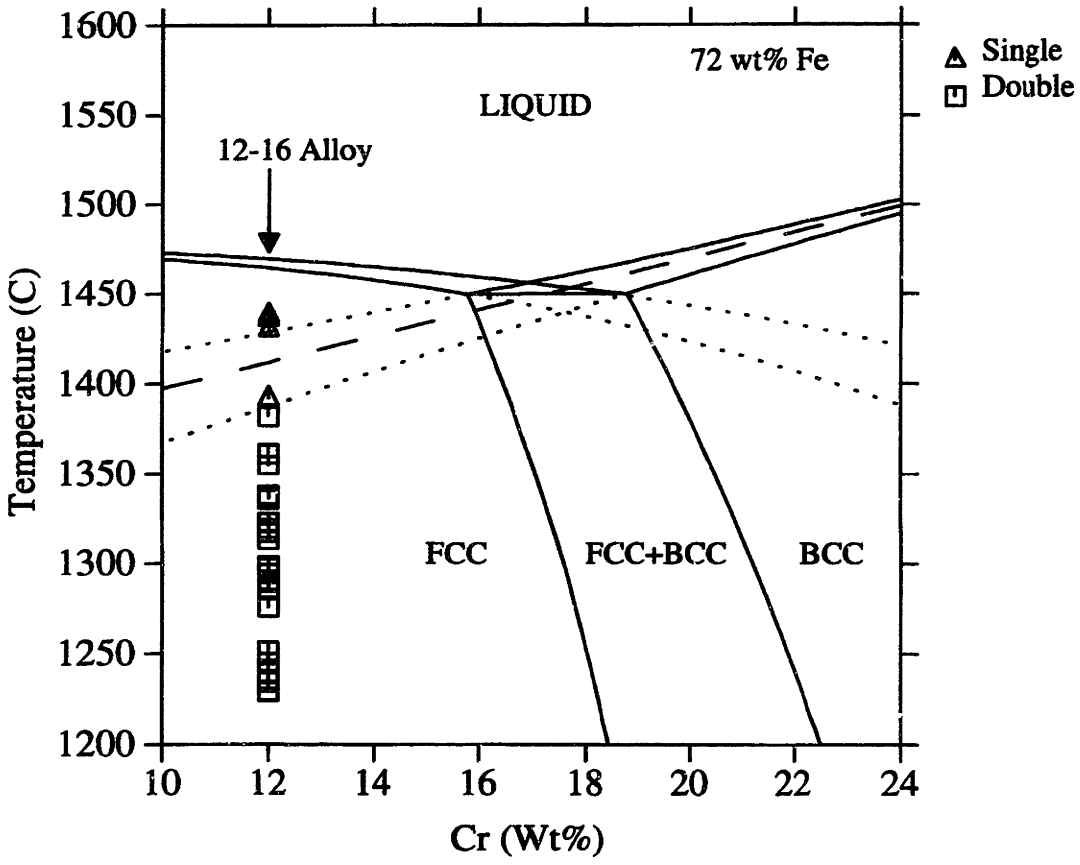

Figure 2-2: Phase selection diagram derived from the space experiments

The T_0 temperature is represented with a dashed line.

Fcc Liquidus T_L^{fcc}	1469.6	C
Fcc Solidus T_S^{fcc}	1464.5	C
T_0^{fcc}	1467.2	C
Heat of fusion ΔH_f^{fcc}	12145.64	J mol^{-1}
Entropy of fusion ΔS_f^{fcc}	6.979043	J mol^{-1} K^{-1}
Partition ratio k_{Cr}	0.888043	
Liquidus Slope m_L^{fcc}	-2.84532	C/Wt%(Cr)
Interfacial energy $\sigma_{liq/fcc}$	0.31305	J m^{-2}

Bcc Liquidus T_L^{bcc}	1428.4	C
Bcc Solidus T_S^{bcc}	1387.4	C
T_0^{bcc}	1411.7	C
Heat of fusion ΔH_f^{bcc}	10803.24	J mol^{-1}
Entropy of fusion ΔS_f^{bcc}	6.416997	J mol^{-1} K^{-1}
Partition ratio k_{Ni}	0.749734	
Liquidus Slope m_L^{bcc}	-6.89934	C/Wt%(Ni)
Interfacial energy $\sigma_{liq/bcc}$	0.22710	J m^{-2}

Table 2.1: Thermodynamic data calculated with Thermo-Calc

Investigator	Alloy	Range of Cr content (Wt%)	Critical Undercooling ΔT^*
Koseki	70wt%Fe-Cr-Ni	15-22	Far below solidus
Volkmann	69wt%Fe-Cr-Ni	1-23	Far below solidus
Moir	69wt%Fe-Cr-Ni	1-23	Far below solidus
Matson (Ground-based)	70wt%Fe-Cr-Ni	15-16	Solidus
Matson (Space)	72wt%Fe-Cr-Ni	12-16	Solidus

Table 2.2: Summary of earlier investigations

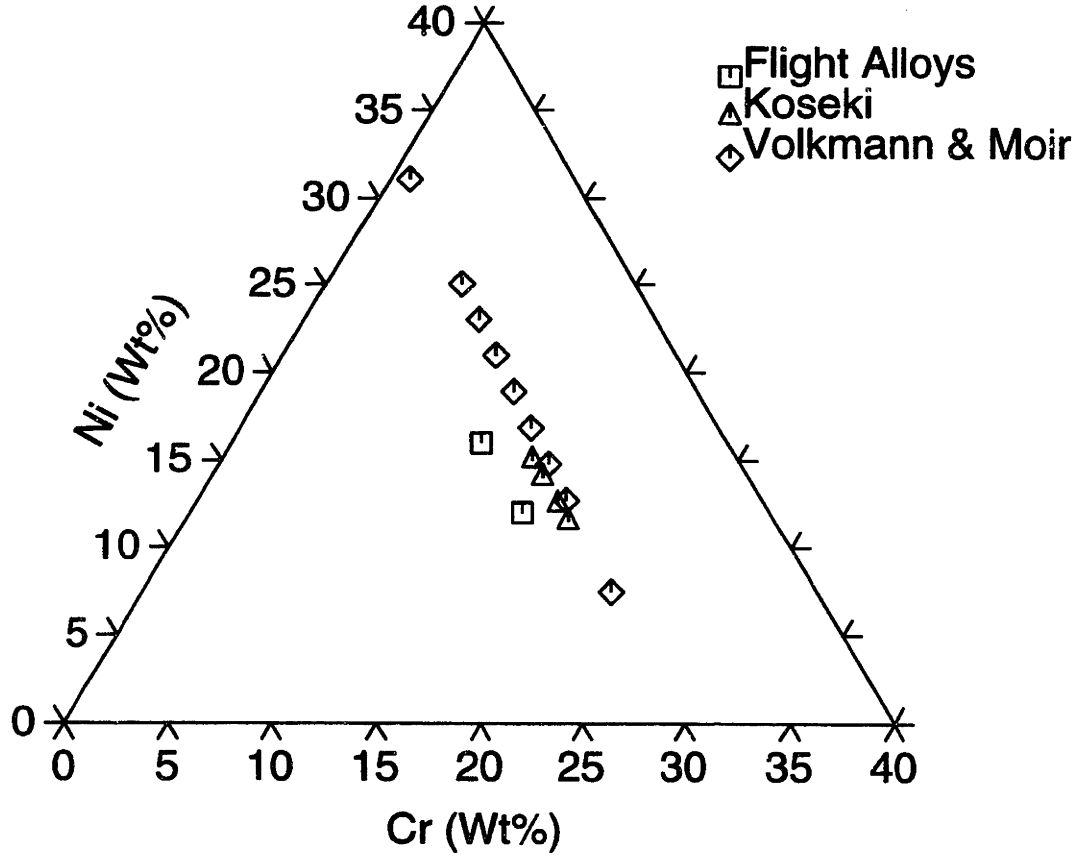

Figure 2-3: Alloy composition of the different investigations

Chapter 3

Experimental Aspects

3.1 Experimental Apparatus

3.1.1 Measurement Instruments

Pyrometer

Temperature measurement was accomplished using a silicon photodiode-based Capintec Series 30 Ratio Pyrometer operating at near infra-red wavelength bands centered at 0.81 and 0.95 microns. It covers a temperature range of 650 C to 2000 C. The gain was set on medium which gave output voltages between 0 V and -3 V. The pyrometer spot size was set to a maximum of 6 mm by fully opening the aperture; thus the entire visible specimen surface was sampled during temperature measurement.

Video Camera

A Kodak Ektapro HS Motion Analyser Model 4540 was used as a high-speed video recording instrument. The system can digitally store, at a rate of 40,500 frames per second, 16,384 images, 64×64 pixel large with 8-bit precision (256 levels of gray) which are subsequently downloaded to the computer in tiff format with the digital download interface provided by the manufacturer.

3.1.2 Data Acquisition

The data acquisition (DAQ) was performed on a 100 MHz HiQ Triton P100 personal computer with 32 MB of RAM running Labview[1] Graphical Programming for Instrumentation version 4.0 for Windows 95[2] and using National Instruments NI-DAQ interface version 5.0. It was equipped with two data acquisition boards; a low-speed board: National Instruments AT-MIO-16E-10 (8 differential channels, 100,000 scans/sec with a resolution of 12 bits) and a high-speed board: National Instruments PCI-MIO-16E-1 (8 differential channels, 1,250,000 scans/sec with a resolution of 12 bits) and a video interface board for the transfer of images from the video camera to the computer: National Instruments AT-GPIB.

3.1.3 Facility

The major components of the system are a vacuum system to pump out fugitive oxygen after each sample loading operation, an inert gas purging manifold to flush the system between runs and provide a source of cooling gas, the electromagnetic levitation facility and finally a sample carousel holding sample holders, nucleation triggers and specimens for processing.

Vacuum System

A vacuum system including a vacuum chamber (approximately 7500 cm^3), a Leybold TMP 150V turbomolecular pump with its backing pump Trivac D8B, a mechanical pump Galileo Vacsound in parallel, two viewports, gas inlets, a gas exhaust, various ports for mechanical manipulators and feedthroughs, and several vacuum gauges was used in order to prevent the oxidation of the material. The ultimate vacuum attained was 10^{-6} Torr between each loading operation.

Inert Gas

Three different kind of gases were used:

- high-purity Argon Grade 5.0 (99.999%) from BOC Gases for purging.
- A mixture of high-purity Argon and 10% Hydrogen by weight from BOC Gases for maintaining a reducing atmosphere during a melt cycle.

[1]Labview is a registered trademark of National Instruments, Inc.
[2]Windows 95 is a registered trademark of Microsoft Corporation.

- A mixture of high-purity Helium and 4% Hydrogen by weight from BOC Gases for cooling.

Levitation Facility

Containerless processing was conducted on an electromagnetic levitation system powered up by a Lepel model T-10-3 High Frequency Induction Heating Unit which is rated at 10 kW at a maximum frequency of 400 kHz. The settings were spin # 14, grid 55 and the power control was varied from 50 to 70 to attain a measured nominal operating frequency of 205 kHz. The split levitation coil used in this experiment had an inner diameter of 16 mm with six lower primary turns in a double loop pattern and two upper reverse-wound turns to augment stability.

Sample Holders

Sample holders were manufactured from high-temperature resistant ceramics to allow manipulation of the specimen within the magnetic field of the coil. Two kinds of ceramic were employed: hot-pressed Boron Nitride (BN) from Carborundum (lot# X54008) and reaction-bonded Silicon Nitride (Si_3N_4) from Goodfellow. Both of these materials present disadvantages. The Boron Nitride may release particles that contaminate specimens and is wet by the liquid metal. The Silicon Nitride is porous and the entrapped gases react with the molten metal. The Boron Nitride sample holders presented a more consistent performance and were used during all experiments.

Nucleation Triggers

Triggers were made from high-purity (99.99%) Nickel and Iron 1 mm diameter wires.

Ni: Materials Research Corporation	lot# i46-0036	($a_0 = 1.24$ Å)
Fe: Leico Industries, Inc.	lot# Fe 49 1010RF	($a_0 = 1.26$ Å)

Samples

Samples were prepared from the master alloy provided by Nippon Steel and used by Koseki [1] (Fe-15 wt% Cr-15 wt% Ni). In order to adjust the composition, pieces of pure Nickel and pure Iron (99.99%) wires were added in-situ, thus converting the composition to Fe-12 wt% Cr-16 wt% Ni. The samples typically weighed 1 g $\pm$ 0.2 and measured

6 mm $\pm$ 0.2. Up to six samples could be processed in a single loading operation by selection from a carousel.

3.2 Experimental Protocol

3.2.1 Undercooling Experiment

Specimens were positioned into the vacuum chamber on individual sample holders placed on a carousel along with nucleation triggers. The system was purged with high-purity Argon three times before it was filled with the mixture of Argon and Hydrogen. During processing, the chamber was maintained at 5 psi above ambient pressure to assure the presence of a reducing gas blanket. The sample was then raised into the coil and power was applied in order to initiate levitation. After stabilizing the specimen with the holder, the holder was removed and the sample was lowered deeper within the bottom half of the coil by reducing the power, thus accelerating heating and inducing melting. Once the sample was fully liquid, power was increased to position the sample in the space between the upper and lower loops of the coil where it was fully visible to the camera and the pyrometer. The sample was further superheated to about 1800 C and subsequently cooled by increasing the flow of the mixture of Helium and Hydrogen. Both spontaneous and triggered nucleation tests were carried out. In the second case, the solidification of the undercooled liquid specimen was induced by touching the surface of the specimen near the bottom with a pure Nickel or Iron stimulation needle.

Throughout the run, the two intensity signals of the pyrometer were recorded by the low-speed DAQ board at a rate of 1 kHz while only one channel was continuously recorded on a buffer (0.5 sec long) by the high-speed board at 500 kHz until triggered. The temperature was calculated real time from those signals using the calibration constants determined from independent calibration experiments (see below). The recalescence event was recorded by both the camera and the high-speed board upon manual triggering following the "flash" due to the sudden rise in temperature. Typical traces from the low and high-speed DAQ boards are shown in Figures 3-1 and 3-2. Digital Pictures were downloaded and stored on the computer in tiff format. Examples can be found in Chapter 4. Between each experiment, the facility was purged with the Argon-Hydrogen mixture. This was desirable in order to change the thermal conductivity of the gas environment such that an adequate

superheat could be achieved during subsequent tests. The dimensions of the major and minor axes were measured and recorded when the facility was opened following completion of all experiments in a run.

3.2.2 Calibration

The calibration technique described by Lum [11] was employed with the improvement that it was conducted with a levitated sample. The same preparation procedure described above was followed. In addition, a Type B thermocouple from Omega was inserted into the sample from the bottom in order to obtain direct temperature measurements. The signal was monitored and recorded on a third channel by the computer through the low-speed board at 1 kHz. Gas cooling was not necessary since the thermocouple acted as a heat sink. To obtain calibration constants, the temperature calculated from the pyrometer signals was matched to the thermocouple trace which was itself adjusted to take into account the temperature loss and the delay in the response of the thermocouple. For more details, refer to [11].

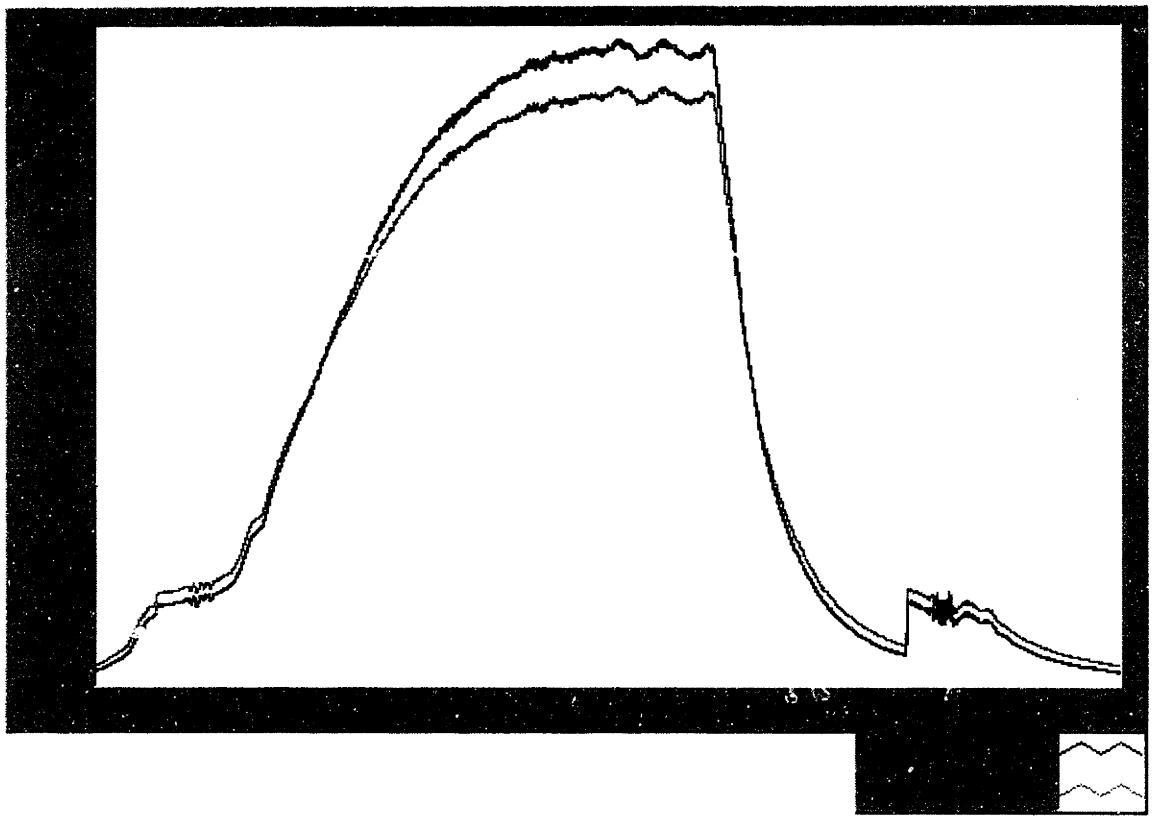

Figure 3-1: Typical low-speed signal (run 22-11)

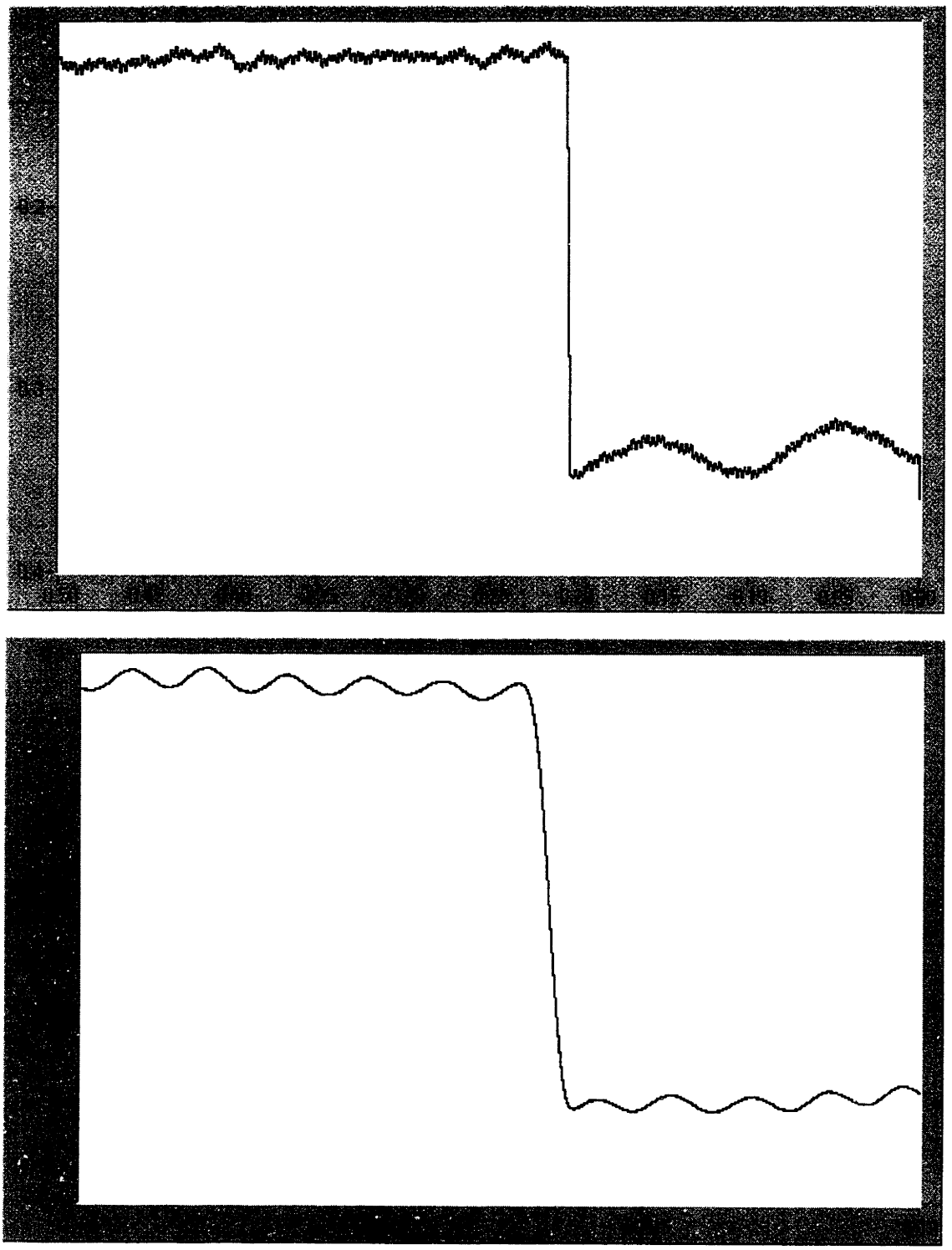

Figure 3-2: Typical high-speed signal (run 22-11)

Chapter 4

Analysis Methods

4.1 Detection of Recalescence

Due to the rapid rise in temperature during the recalescence phenomenon, a characteristic "flash" was observed and consequently allowed manual triggering of the high-speed sensors. The discrimination between a double and a single event was performed by video analysis following the test using the method presented in Reference [10]. The occurrence of a double recalescence event could theoretically be detected by high-speed pyrometry as well [2, 6]. However, it can be seen from Figure 3-2 on page 24 which shows the high-speed signal recorded during run 22-11 (a test which exhibits a double recalescence as apparent in Figure 4-6) that such was not the case in the present study.

4.2 Temperature

The undercoolings were calculated using one-color pyrometry on the high-speed signal of the pyrometer. The modified form of Planck's Law using Wien's approximation yields:

$$I = k_\lambda \exp(-\frac{C_2}{\lambda T_b})$$

where:

- I is the intensity.
- k_λ is an instrument constant.

- C_2 is Planck's second constant.
- λ is the effective wavelength: 0.81 microns.
- T_b is the black body temperature.

This can be transformed into:

$$\ln(\frac{I}{I_0}) = -\frac{C_2}{\lambda}(\frac{1}{T} - \frac{1}{T_0}) + \ln(\frac{\epsilon}{\epsilon_0})$$

where:

- T and T_0 are the radiance temperatures relative to the intensities I and I_0 respectively.
- ϵ and ϵ_0 are the corresponding spectral emissivities (it was assumed here that $\epsilon = \epsilon_0$).

The temperature was also recovered from the two-color pyrometer low-speed signals and the calibration constants using a linear relationship as explained in Reference [11]:

$$T = K(R - R_0) + T_0$$

where T_0 is the liquidus of the fcc phase and R_0 is the signals' ratio at this reference temperature.

Calibration tests resulted in a value of K=1600 K/unit of ratio and a typical value for R_0 of 0.889 ± 0.05 evaluated at the melt plateau. A good match was observed when comparing undercoolings obtained using these two methods. From these results, a precision of $\pm$ 5 K in temperature measurement is proposed.

4.3 Video Analysis

Successive tiff images were sequentially ordered using a Labview[1] virtual instrument (VI) to generate a video movie. By observing the long duration motion of the sample, the motion and orientation of the droplet could be defined and mathematically described using matrix algebra assuming an ellipsoidal droplet shape. Major and minor axis dimensions were measured post-test. Using this technique, the trajectory of specific surface elements

[1]Labview is a registered trademark of National Instruments, Inc.

was tracked within the image as a function of time. Examples of tiff images can be seen in Figure 4-1, 4-2, 4-3, 4-4 and 4-5.

4.3.1 Delay Time

The delay times were evaluated from the video in the same manner described in Reference [10] by measuring the time between the successive rises in intensity of a given individual pixel as illustrated in Figure 4-6. Emissivity measurements as a function of temperature, phase and composition for ternary steel alloys show that the temperature rise accompanying recalescence is visible on the video image as a corresponding rise in broadband emissive intensity: hotter is brighter. By tracking the changes in intensity for a selected surface element over time, the existence of localized double recalescence events may be confirmed to a resolution on the order of the size of a single pixel. For these tests, typical pixel dimensions corresponded to a square surface element 200 μm in projected width.

4.3.2 Velocity

The velocity of the tip of the dendrite array was calculated using an imaging method detailed in Reference [10]. In brief, the leading edge of the array was tracked by observing the location of the interface between the dark and undercooled liquid and the bright primary solid as growth proceeded across the surface. On each image, the two-dimensional coordinates of selected interface pixel were converted into three-dimensional spatial coordinates using a Labview VI. Recursive iteration over space and time allowed prediction of the best-fit nucleation site based on droplet shape and motion. Since the array propagates through the sample with a preferred direction of growth and since the orientation of this front relative to the droplet surface could be defined from the video record, the tip propagation velocity was readily calculated using a spherical growth model.

In other instances, the tip velocity was defined as the chord distance between the location where nucleation initiated and the location where the array tip intersected the sample surface (typically diametrically opposite the nucleation site) divided by the transit time (as derived from frame count). Figure 4-4 shows a recalescence event where nucleation initiated at the base of the droplet and the array tip clearly emerges at the top.

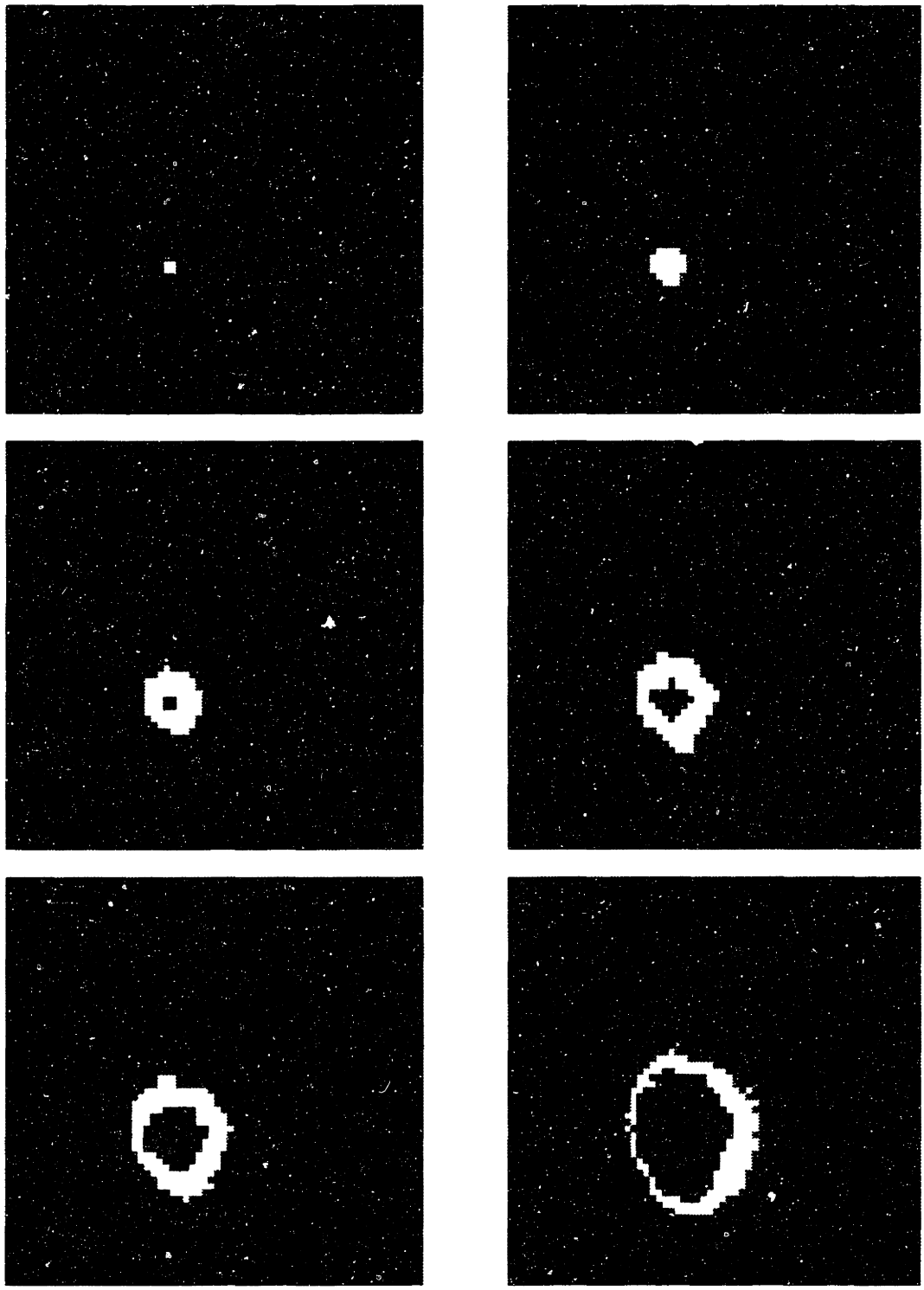

Figure 4-1: Digital images showing a central secondary nucleation

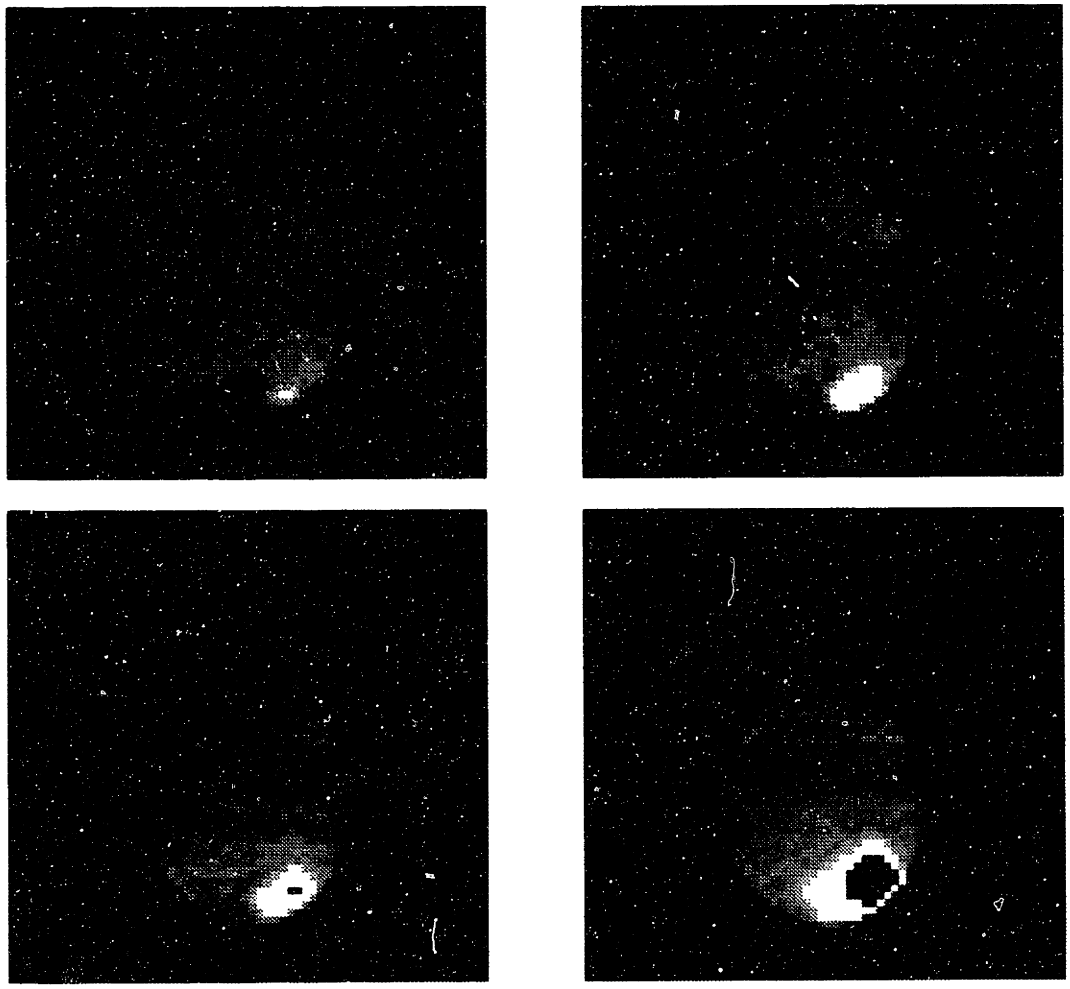

Figure 4-2: Digital images showing a semi-solid secondary nucleation

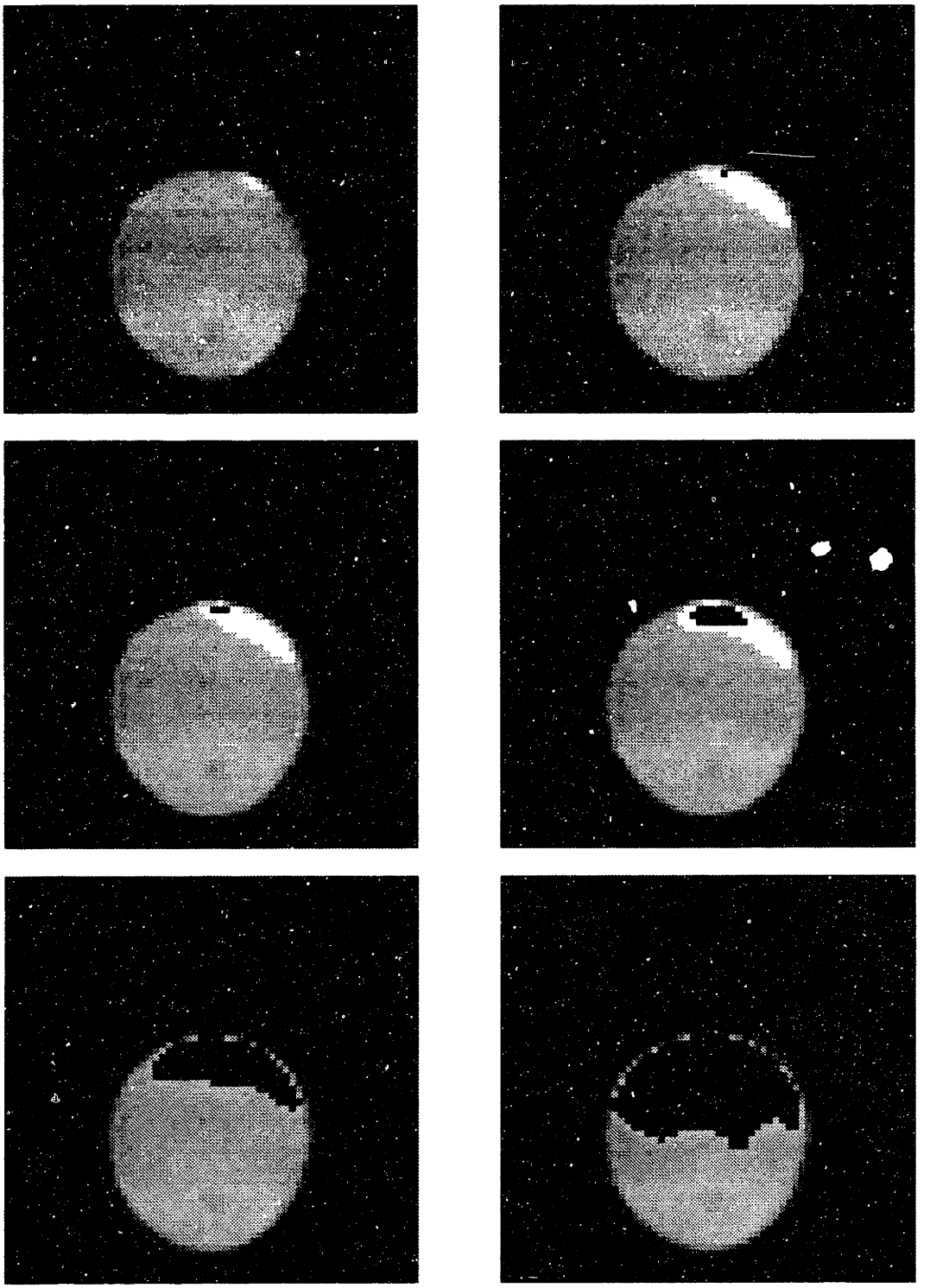

Figure 4-3: Digital images showing an edge secondary nucleation

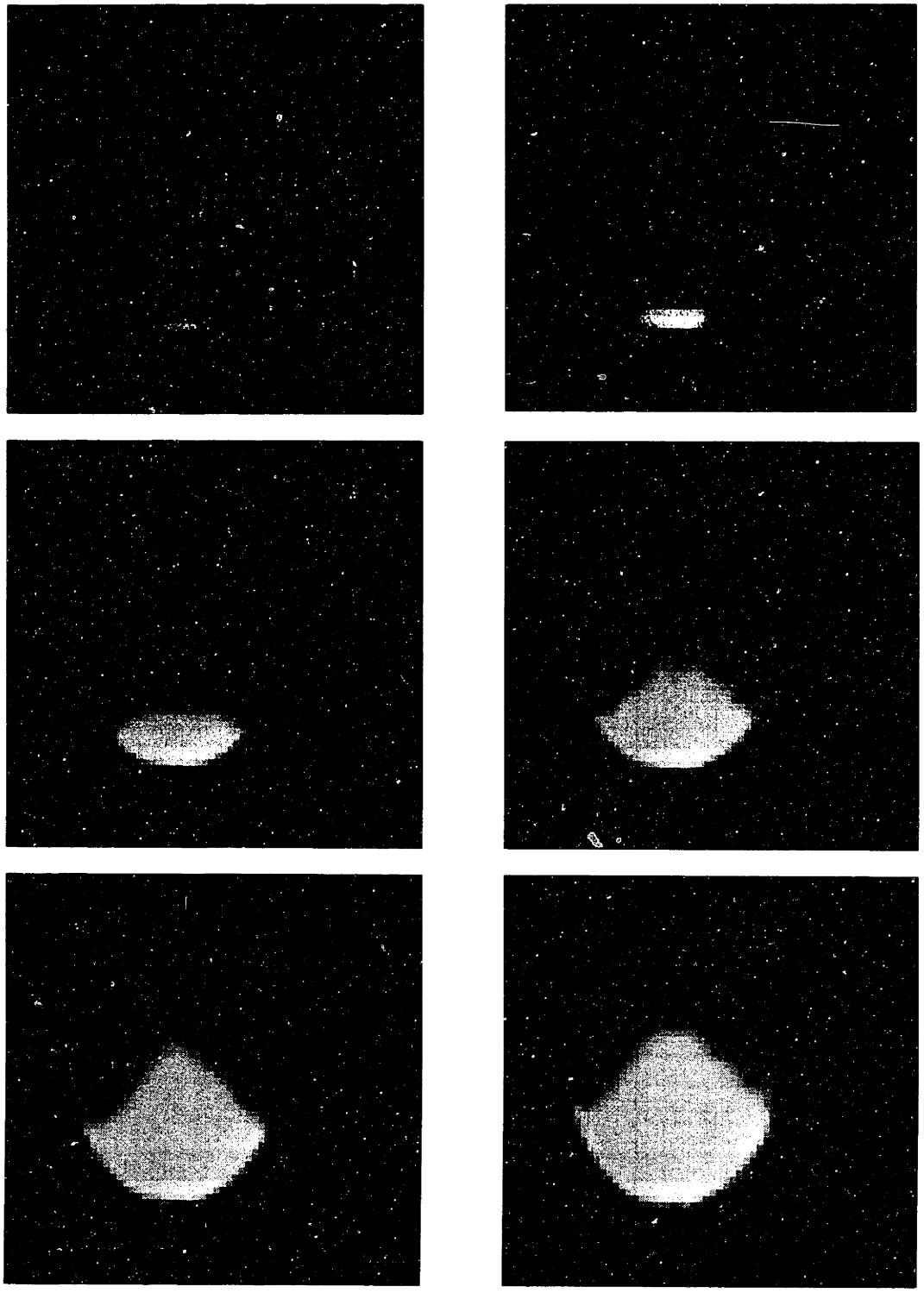

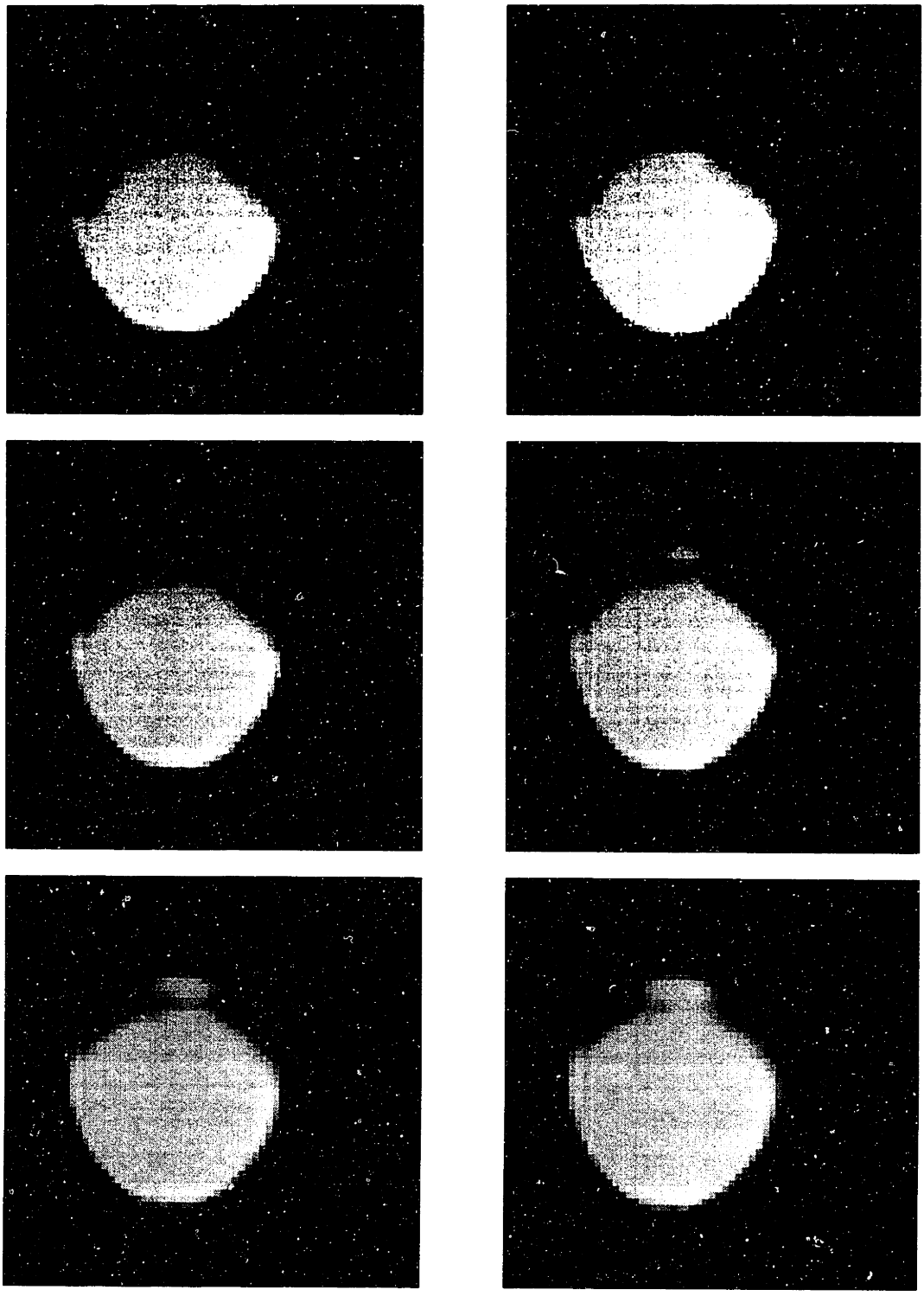

Figure 4-4: Digital images showing the emergence of the array tip

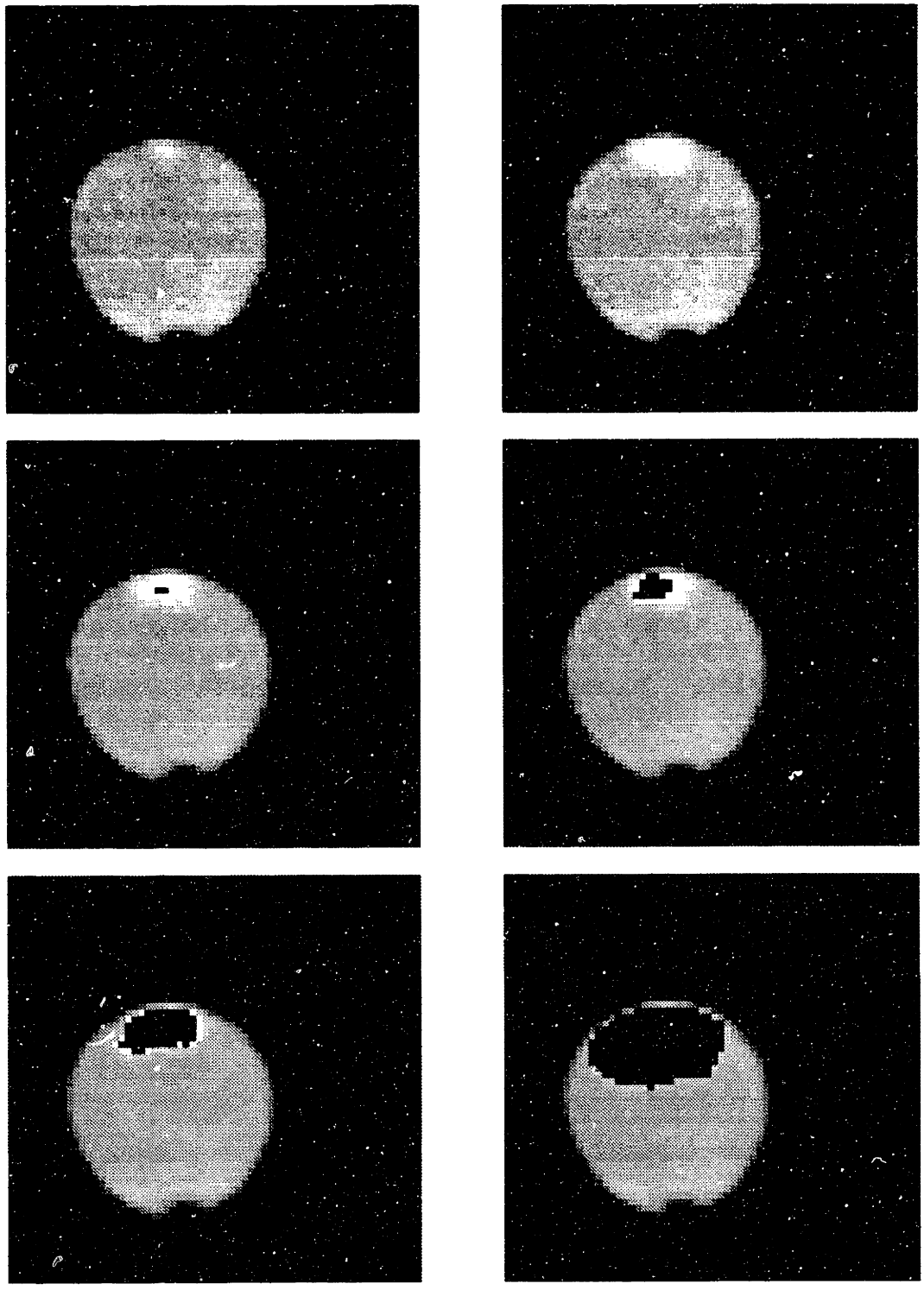

Figure 4-5: Digital images showing the overwhelming of the primary bcc phase

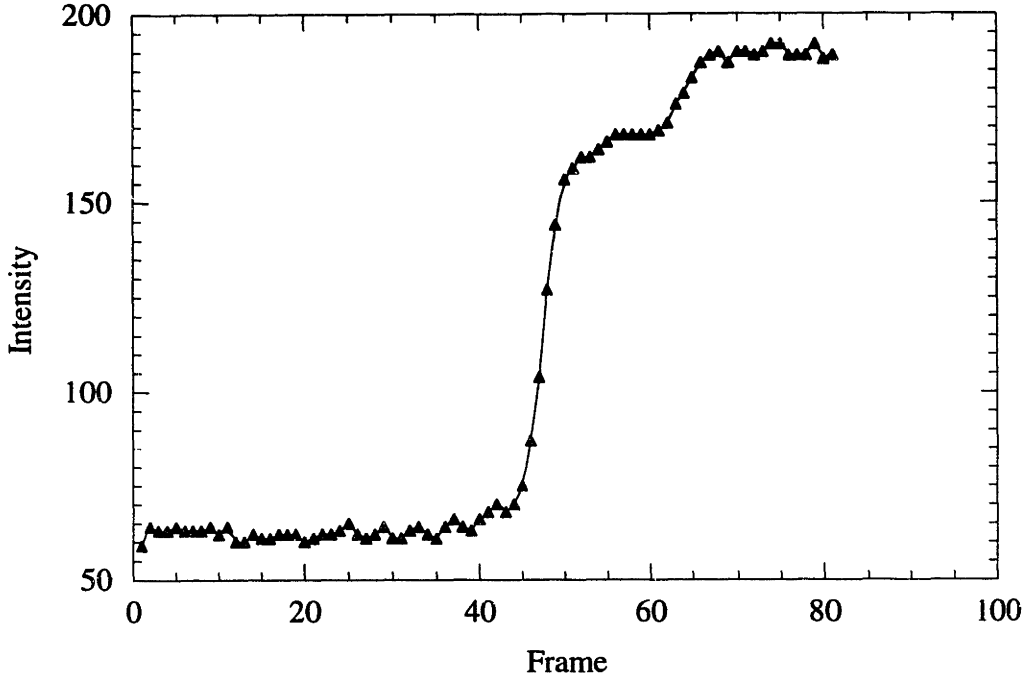

Figure 4-6: Typical intensity profile (run 22-11)

Chapter 5

Results

5.1 Definitions

5.1.1 Undercooling

Undercoolings were evaluated based on the difference between the bulk fluid temperature at nucleation and the liquidus of the equilibrium fcc phase.

The critical undercooling $\Delta T''$ was defined as the lowest undercooling necessary to obtain a double recalescence event with reference to the liquidus temperature of the γ phase. The critical transition temperature T'' corresponding to $\Delta T''$ is thus defined by: $\Delta T'' = T_L^{fcc} - T''$.

5.1.2 Location of Secondary Nucleation

Confirming observations made by Matson [10], three mechanisms were identified for the location of the secondary nucleation event:

S_1 at the primary nucleation site.

S_2 elsewhere within the semi-solid region formed by the growth of the primary δ.

S_3 on the edge of the semi-solid region.

Illustrations of these types of secondary nucleation are shown in Figures 4-1, 4-2 and 4-3 in Chapter 4 where the primary metastable δ phase is represented in yellow and the secondary equilibrium γ phase in red.

5.1.3 Delay Time

Four types of delay time were of interest:

τ_1 Taken at the common primary and secondary nucleation location, delay time between the two nucleations.

τ_2 Taken at an adjacent secondary nucleation location within the semi-solid region, delay time between the passage of the primary bcc front and the nucleation of the secondary fcc phase.

τ_3 Taken at the primary nucleation location, delay time between the nucleation of the metastable bcc phase and the passage of the secondary fcc front (applies to edge nucleation and semi-solid nucleation)

τ_4 Taken at an arbitrary spot, delay time between the passage of the primary bcc front and the passage of the secondary fcc front. (Only available data from an event where nucleation occurred out of the field of view)

5.1.4 Velocity

Following the classification proposed by Matson [10], three velocities were measured:

$V_{\delta \to L}$ velocity of the bcc phase growing into the undercooled liquid.

$V_{\gamma \to L}$ velocity of the fcc phase growing into the undercooled liquid.

$V_{\gamma \to \delta}$ velocity of the fcc phase growing into the semi-solid mixture of δ and liquid.

5.2 Overview

Table 5.1 gives a summary of relevant information which define key experimental results for each run. The possible analyses on the mechanism of secondary nucleation, delay time and velocity were categorized by the criteria above.

5.3 Delay Time

The delay time results determined by video analysis are presented in Table 5.2. Delay times were obtained by looking at the intensity of individual pixels as a function of time which

exhibits two successive rises in the case of a double recalescence event. Five delay times were measured, corresponding to τ_1, τ_2, τ_3 and a minimum and a maximum value of τ_4.

5.4 Velocity

Table 5.3 presents the results of velocity calculations from the high-speed video record. As noted earlier, two different calculation methods were employed. In the first method, a model based on spherical expansion of the front was used to back calculate the nucleation time and position from the interface position in each frame. In the second method, this nucleation position was subsequently used to calculate the chord distance to the point where the array intersects the droplet surface under conditions of bulk tip propagation. Using these methods, it was possible to measure the three different propagation velocities discussed previously. Nucleation triggering was conducted using stimulation needles fabricated from either fcc pure Nickel or bcc pure Iron. In the event that no stimulation needle was used, the model predicted that spontaneous nucleation occurred at a random position on the surface of the droplet. These events are indicated by dashes in the trigger column of the table.

						Analyses	
Run	Alloy	Trigger	ΔT (C)	Type	Nucleation	Velocity	Delay Time
27-11	12-16	–	53	Single	Back	–	–
27-10	12-16	–	29	Single	Front	γ	–
27-9	12-16	Fe	69	Single	Front	γ+	–
27-8	12-16	Fe	113	Single	Front	γ	–
27-7	12-16	Fe	77	Single	Front	γ+	–
27-6	12-16	–	138	Double (Primary)	Front	δ+,Semi-solid+	τ1,τ2,τ4
27-5	12-16	–	53	Double (Back Internal)	Front	δ–,Semi-solid+	τ3,τ4
27-4	12-16	Fe	145	Double (Primary)	Front	δ+,Semi-solid+	τ1,τ4
27-3	12-16	–	46	Single	Front	γ–	–
27-2	12-16	–	44	Single	Back	–	–
27-1	12-16	–	10	Single	Front	γ–	–
26-1	12-16	–	91	Double (Internal)	Back	–	τ4
25-4	12-16	–	77	Single	Back	–	–
25-3	12-16	–	170	Double (Internal)	Back	–	τ4
25-2	12-16	–	192	Double (Primary)	Front	δ–,Semi-solid–	τ1,τ2,τ4
25-1	12-16	–	83	Single	Back	–	–
22-11	12-16	Fe	159	Double (Primary)	Front	δ–,Semi-solid–	τ1,τ4
22-10	12-16	–	54	Double (Edge)	Front	δ–,γ–,Semi-solid–	τ2,τ3,τ4
22-9	12-16	Fe	38	Single	Front	γ–	–
22-8	12-16	–	74	Double (Edge)	Back	γ–,Semi-solid–	τ4
22-7	12-16	–	117	Double (Internal)	Back	–	τ4
22-6	12-16	Fe	146	Double (Primary)	Front	δ+,Semi-solid–	τ1,τ4
22-5	12-16	–	201	Double (Internal)	Back	–	τ4
22-4	12-16	–	215	Double (Internal)	Back	–	τ4
22-3	12-16	–	49	Double (Primary)	Front	δ–,γ–,Semi-solid–	τ1,τ2,τ4
22-2	12-16	–	50	Single	Top Edge	γ–	–
22-1	12-16	Fe	65	Single	Front	γ–	–
21-7	12-16	Ni	70	Single	Front	γ–	–
21-6	12-16	Ni	80	Single	Front	γ–	–
21-5	12-16	Ni	145	Single	Front	γ–	–
21-4	12-16	Ni	152	Single	Front	γ–	–
21-3	12-16	Ni	36	Single	Front	γ+	–
21-2	12-16	Ni	108	Single	Front	γ+	–
21-1	12-16	Ni	143	Single	Front	γ–	–
20-18	12-16	–	182	Double (Internal)	Back	–	τ4
20-17	12-16	–	227	Double (Internal)	Back	–	τ4
20-16	12-16	–	178	Double (Edge)	Back	–	–
20-15	12-16	–	61	Single	Back	–	–
20-14	12-16	–	62	Single	Back	–	–
20-13	12-16	–	77	Single	Back	–	–
20-12	12-16	–	54	Single	Back	γ	–
20-11	12-16	–	112	Double (Primary)	Front	δ–,Semi-solid–	τ1,τ2,τ4
20-10	12-16	–	202	Double (Internal)	Back	–	τ4
20-9	12-16	–	79	Single	Top Edge	γ	–
20-8	12-16	–	204	Double (Internal)	Back	–	τ4
20-7	12-16	–	189	Double (Internal)	Back	–	τ4
20-6	12-16	–	47	Single	Back	–	–
20-5	12-16	–	37	Single	Back	–	–
20-4	12-16	–	138	Double (Internal)	Back	–	τ4
20-3	12-16	–	105	Single	Back	–	–

20-2	12-16	–	64	Single	Back	–	–
20-1	12-16	–	59	Single	Top Edge	γ–	–
19-7	12-16	–	199	Double (Internal)	Back	–	$\tau 4$
19-6	12-16	–	80	Single	Top Edge	γ–	–
19-5	12-16	–	214	Double (Primary)	Front	δ–	$\tau 1$,$\tau 4$
19-4	12-16	–	189	Double (Internal)	Back	–	$\tau 4$
19-3	12-16	–	193	Double (Internal)	Back	–	$\tau 4$
19-2	12-16	–	54	Single	Back	–	–
19-1	12-16	–	135	Double (Internal)	Back	–	$\tau 4$
18-11	12-16	–	75	Single	Back	–	–
18-10	12-16	–	150	Double (Internal)	Back	–	$\tau 4$
18-9	12-16	–	189	Double (Internal)	Back	–	$\tau 4$
18-8	12-16	–	223	Double (Internal)	Back	–	$\tau 4$
18-7	12-16	–	143	Double (Internal)	Back	–	$\tau 4$
18-6	12-16	–	182	Double (Internal)	Back	–	$\tau 4$
18-5	12-16	–	48	Single	Back	–	–
18-4	12-16	–	25	Single	Front	γ–	–
18-3	12-16	–	81	Double (Internal)	Back	–	$\tau 4$
18-2	12-16	–	37	Single	Back	–	–
18-1	12-16	–	196	Double (Internal)	Back	–	$\tau 4$
17-2	12-16	–	192	Double (Internal)	Back	–	$\tau 4$
17-1	12-16	–	90	Double (Internal)	Back	–	$\tau 4$
16-12	12-16	–	182	Double (Internal)	Back	–	$\tau 4$
16-11	12-16	–	172	Double (Edge)	Back	–	–
8-1	12-16	–	–	Single	Back	–	–
6-4	12-16	–	43	Single	Back	–	–
6-3	12-16	–	44	Single	Back	–	–
6-2	12-16	–	35	Single	Front	γ–	–
6-1	12-16	–	27	Single	Front	γ–	–
4-3	12-16	–	28	Single	Back	–	–
4-2	12-16	–	–	Single	Front	γ–	–
4-1	12-16	–	–	Single	Front	–	–
3-1	12-16	–	–	Single	Back	–	–

Table 5.1: Summary of all experiments

Run	ΔT (C)	τ1 (μs)	τ2 (μs)	τ3 (μs)	τ4 min (μs)	τ4 max (μs)
27-6	138	296	148		222	420
27-5	53			4691	198	
27-4	145	148			198	420
26-1	91				173	420
25-3	170				148	420
25-2	192	173	148		173	370
22-8	74					1333
22-7	117				198	494
22-6	146	222			247	370
22-5	201				222	444
22-4	215				123	395
22-3	49	1728	1481			
22-11	159	198				370
22-10	54		938	1383		1407
20-8	204				173	420
20-7	189				148	346
20-4	138				99	519
20-18	182				173	346
20-17	227				99	395
20-11	112	296	148		222	420
20-10	202				148	395
19-7	199				741	1309
19-5	214	99			99	395
19-4	189				123	321
19-3	193				148	519
19-1	135				667	1605
18-9	189				148	469
18-8	223				123	321
18-7	143				469	1901
18-6	182				123	395
18-3	81				99	1432
18-10	150				173	420
18-1	196				99	395
17-2	192				148	444
17-1	90				123	667
16-12	182				148	296

Table 5.2: Tabulated delay time data

Run	Trigger	ΔT (C)	V δ -> L (m/s)	V γ -> L (m/s)	V γ -> δ (m/s)	V tip δ (m/s)	V tip γ (m/s)
27-10	-	29		1.6			
27-9	Fe	69		6.4			9.3
27-8	Fe	113		16.2			
27-7	Fe	77		10.9			12.6
27-6	-	138	8.3		6.5	8.8	
27-5	-	53	1.6				
27-4	Fe	145	11.2		7.5		
27-3	-	46		4.5			
27-1	-	10		0.7			
25-2	-	192	14.8		7.1		
22-11	Fe	159	9.1		7.6	13.6	
22-10	-	54	1.9	4.2			
22-9	Fe	38		1.6			1.9
22-8	-	74	2.4	7.8			10.5
22-6	Fe	146	8.2		6.1	10.9	
22-3	-	49	1.9	4.3	6.9		
22-2	-	50		3.3			
22-1	Fe	65		5			5.7
21-7	Ni	70		5.9			
21-6	Ni	80		8.6			
21-5	Ni	145		36.6			
21-4	Ni	152		36.3			
21-3	Ni	36		1.4			2.2
21-2	Ni	108		13.7			16.5
21-1	Ni	143		28.1			
20-11	-	112	6.9		6.8		
19-5	-	214	27.4				

Table 5.3: Tabulated velocity data

Chapter 6

Discussion

6.1 Phase Selection

The 72 wt% Fe isopleth and the thermodynamic properties of the alloy were evaluated using Thermo-Calc version L (database SGTE solution 1992). The calculated pseudo-binary diagram is shown in Appendix A-1 and the data in Table 2.1.

The space results presented in Figure 2-2 [9] suggest that the critical undercooling necessary for the nucleation of the metastable bcc phase corresponds to its solidus temperature. This contradicts the ground-based results of Koseki [2], Volkmann [6] and Moir [7] who reported independently that a much deeper undercooling was required in order to observe a double recalescence. However this is in agreement with ground-based velocity results from Matson [10]. The ground-based results presented here indicate that the critical undercooling $\Delta T''$ lies even higher: at the T_0 temperature of the δ phase, as shown in Figure 6-1. It can be seen in that figure that spontaneous double recalescence events were observed up to the calculated T_0 temperature of the bcc phase represented by a dashed line. Therefore the critical undercooling $\Delta T''$ for the Fe-12 wt% Cr-16 wt% Ni alloy studied is equal to:

$$\Delta T'' = T_L^{fcc} - T_0^{bcc} = 58\ C$$

Furthermore, in this work, double recalescence was never detected by high-speed pyrometry but only by the high-speed video camera, which suggest that equipment limitations probably prevented other investigators from detecting double recalescence events at lower undercoolings.

The nature of the trigger appears to have a decisive influence on phase selection. Over the same range of undercoolings, approximately from 40 C to 150 C, no double recalescence events were observed during the seven tests when nucleation was triggered with an fcc Nickel needle as opposed to three out of eight with a bcc Iron trigger, as can be seen in Table 5.1 and Figure 6-1. Despite the fact that a double recalescence event could have appeared as a single event due to the limited detection resolution, these statistics strongly suggest that there is a difference in behavior between fcc and bcc triggers, which stands in disagreement with conclusions from Moir [7].

6.2 Delay Time

Ground-based results on delay times obtained by a video technique are shown in Figure 6-2. Despite the large scatter, the data typically lies between two average extreme values represented by horizontal lines. Figure 6-3 compares the delay time results from ground-based experiments, represented by a box and space experiment where ZPY refers to the data of the ZPY pyrometer, adjacent to the trigger and RAD to that of the RAD pyrometer positioned at a right angle. It can be seen that they follow the same trend and fall in good agreement. Note however that the ground-based results are slightly lower than those in space. This might be due to the effect of convection on the secondary nucleation mechanism. The dependence of delay times on the alloy composition is illustrated in Figure 6-4.

6.3 Velocity

The velocity of an isolated dendrite tip growing into the undercooled liquid was calculated using the LKT model presented in Reference [12]. The code was written in Maple[1] V release 4 and is included in Appendix B.

Previous velocity results taken from Volkmann [6] at a Ni/Cr atomic ratio of 1.067 and from Moir [7] at a Ni/Cr ratio of 1.385 are shown in Figure 2-1. This data indicates that at a constant Iron content of 69 wt% Fe, the effect of the relative concentration of the two solute elements on the growth velocity is limited for both the δ and γ phases. In either case, the growth velocity of the metastable phase is significantly smaller than that of the

[1]Maple is a registered trademark of Waterloo Maple Software.

stable phase. On this curve, the critical undercooling ΔT_{crit} is marked by a vertical arrow; at undercoolings below this value, double recalescence was not observed.

Figure 6-5 shows the results obtained for a nominal 12-16 alloy in ground-based testing and in micro-gravity experiments aboard the space shuttle. For this alloy, the Ni/Cr atomic ratio is 1.181 for a composition based on 72 wt% Fe. From this figure, it is apparent that there is no significant difference in velocities measured for growth of the metastable δ phase between ground-based and space-processing environments. Comparing these results to those in Figure 2-1, it is clear that a significant difference in velocity is seen even for small changes in total solute concentrations as indicated by the increase from 69 to 72 wt% Fe.

For the 12-16 alloy, the stable phase growth could be measured for growth into either virgin undercooled liquid or the semi-solid mixture of metastable δ and residual liquid following the primary solidification during double recalescence. The growth of γ is shown in Figure 6-6. Note that the propagation velocity of the stable phase into the semi-solid appears independent of the original undercooling and extends over the range: 49 C $< \Delta T <$ 192 C.

During primary recalescence, the metastable phase grows into the virgin undercooled liquid and forms a semi-solid mixture of δ and liquid which is heated to the temperature of the intermediate plateau. After a certain delay, the second recalescence event occurs and growth of the stable phase takes place into this mixture. If the temperature of the intermediate plateau is independent of the original liquid undercooling, as reported by Koseki [2] and Volkmann [6], it is not surprising that the growth velocity of the stable phase during the second recalescence event is also independent of the original undercooling as shown by Matson [10]. This value is, however, a strong function of the alloy composition since Matson found a constant average $V_{\gamma \rightarrow \delta} = 2$ m/s for a 15-15 alloy while this study shows an average $V_{\gamma \rightarrow \delta} = 6.9$ m/s for a 12-16 alloy. It is suggested that this composition dependence is linked to the composition dependence of the T_0 temperatures of the fcc and bcc phases. As the composition approaches the eutectic composition, the gap between the two T_0 temperatures decreases, therefore the apparent undercooling seen by the γ phase growing into the δ phase decreases; growth should thus occur at a lower velocity. At the lowest undercooling, the growth into the semi-solid is slightly faster than the growth into the undercooled liquid, indicating that the preexistence of a metastable semi-solid network may accentuate the growth of the stable phase.

Figure 6-7 shows the growth velocity of the metastable phase compared to that of the

stable phase growing into the semi-solid mixture. Since the growth of the metastable phase into the liquid during primary recalescence could be measured prior to the formation of the stable phase within this transformed material, there is usually a one-to-one comparison between these two growth conditions. In this figure, the critical undercooling value at cross-over, ΔT_X, is defined as corresponding to the point where the two propagation velocities are equal:

$$V_X = V_{\delta \rightarrow L} = V_{\gamma \rightarrow \delta}$$

where all are a function of composition. For the 12-16 alloy, the cross-over undercooling is found to be: $\Delta T_X = 132$ C. Below this critical undercooling value, the growth of the stable phase into the semi-solid is faster than that of the metastable phase into the virgin liquid. Therefore, the stable phase can overwhelm the growing metastable phase and break-out into the undercooled liquid. This is seen in the mosaic of images presented in Figure 4-5. After break-out, the apparent undercooling seen by the growing stable phase is much greater than within the semi-solid region and the front velocity exhibits a change in propagation rate. Depending on the original undercooling, the γ phase can either slow down once it reached the undercooled liquid (for $\Delta T'' < \Delta T < 70$ C) or show an increase in growth velocity (for 70 C $< \Delta T < \Delta T_X$). This fact is illustrated in Figure 6-6.

As noted earlier, the range of undercoolings observed can be seen to extend down to a minimum which corresponds to a temperature approaching the metastable phase T_0 temperature. It is apparent from Figure 6-7 that at undercoolings between $\Delta T''$ and ΔT_X, double recalescence events may appear only as single events because break-out occurred before the primary front reached the area seen by the sensor. To emphasize this point, the critical velocity V_{crit} for propagation of the δ phase is evaluated from the previous investigations at the reported critical undercooling ΔT_{crit} and plotted as a function of the Ni/Cr ratio in Figure 6-8. This velocity appears to be insensitive to the Iron content since the data from all investigators fall onto a common curve.

It is expected that the velocity of the metastable phase measured at the critical undercooling ΔT_{crit} would be less than that predicted by the cross-over undercooling: $V_{crit} < V_X$. This is explained by the fact that the stable front growing into the semi-solid must propagate significantly faster in order to catch up with the metastable front given that the metastable phase has had the advantage of growth during the delay time between the two nucleation

events. This can be seen by the difference between the prediction of V_{crit} based on the curve in Figure 6-8 and the observed V_X plotted as an average value with error bars in the same figure. Consequently, the reported critical undercooling, ΔT_{crit}, also differs from the cross-over undercooling ΔT_X. If a model can be developed to quantify the deviation as a function of sensor geometry, it should be possible to predict the observed critical undercooling and velocity based on the alloy cross-over point and delay times.

6.4 Mechanism for Secondary Nucleation

Results from both spontaneous and triggered nucleation tests seem to suggest that internal secondary nucleation illustrated in Figure 4-1 is preferred over the edge nucleation mechanism shown in Figure 4-3 since out of a total of thirty-eight reported double recalescence events, only four clearly exhibit an edge secondary nucleation. However, it is hypothesized that the actual number of edge secondary nucleation events for ground-based testing is greater than the one observed. As pointed out previously, at all undercoolings, the growth of the equilibrium γ into the undercooled liquid is faster than that of the metastable δ into the liquid, thus enabling the fcc phase to overwhelm the primary bcc during an edge nucleation event which would therefore be seen as a single recalescence event. At the same time, above the cross-over undercooling ΔT_X, the propagation velocity of the primary δ is greater than that of the secondary γ into the semi-solid:

$$V_{\delta \to L} > V_{\gamma \to \delta}$$

A central nucleation event would therefore always be detected as such. This defines a region where central and edge nucleation events can be differentiated. At undercoolings below the cross-over point, the detection of a central event also depends on the position of the sensor relative to the nucleation site. In some instances, like edge nucleation events, central nucleation events would appear as single recalescence events; it would therefore not be possible to distinguish between the two nucleation mechanisms. This fact also explains the previous observations of a depressed critical undercooling for the nucleation of the metastable phase. It is then clear that the geometry of the system has a critical influence on the observed results. A simple model is proposed below to account for the discrepancy between the conclusions of the various investigations.

6.5 Model for Central Nucleation

A model for the central nucleation event was developed and is presented in this section.

In the case of a central nucleation event, the relationship between the delay time observed at the common primary and secondary nucleation site, τ_1 and the delay time observed at an arbitrary location at a distance L, τ_4 is given by:

$$\tau_4 = \tau_1 + L(\frac{1}{V_{\gamma\to\delta}} - \frac{1}{V_{\delta\to L}}) \tag{6.1}$$

Therefore, given certain growth velocity conditions $V_{\gamma\to\delta}$ and $V_{\delta\to L}$, the critical distance L_{crit} at which the secondary fcc front catches up with the primary bcc front ($\tau_4 = 0$) is given by:

$$L_{crit} = \frac{V_{\delta\to L}\tau_1}{1 - \frac{V_{\delta\to L}}{V_{\gamma\to\delta}}} \tag{6.2}$$

The calculations based on the average extreme values of the delay time are plotted in Figure 6-9 and give best and worst-case scenarii.

Conversely, it can be seen from Equation 6.1 that at a given distance L from the nucleation site, there is a critical velocity for the growth of the metastable phase where $\tau_4 = 0$, i. e. the secondary fcc front catches up with the primary bcc front at that location. If triggering was done at the base of the droplet and detection was performed at a right angle, assuming a dendrite array tip angle of 90 degrees, the critical lengthscale L_{crit} is equal to the diameter of the droplet, approximately 6 mm. In that case, this critical velocity should correspond to the critical velocity V_{crit} mentioned earlier and shown in Figure 6-8 as a function of composition. The best and worst-case scenarii of Figure 6-9 give values for the critical undercooling, ΔT_{crit} at this value of L_{crit} of: 99 C and 119 C respectively. The velocities of δ corresponding to these undercoolings are, from Figure 6-7: 4.1 m/s and 5.6 m/s respectively. As expected, these values lie on either side of the critical velocity predicted for the 12-16 alloy by Figure 6-9: 4.35 m/s and both are lower than the observed cross-over velocity $V_X = 6.9$ m/s.

It is theoretically possible to calculate the cross-over velocity V_X from the critical velocity V_{crit} observed by pyrometry with Equation 6.2 given good delay time and velocity measurements.

Note that the model is solely valid for central nucleation and breaks down in the case of semi-solid and edge nucleation which have been observed during ground-based testing (see Figures 4-2 and 4-3).

6.6 Consequence on 1-g and micro-gravity behaviors

As discussed above, at temperatures below its T_0 temperature, the nucleation of the δ phase is possible and will occur unless phase selection by choice of trigger material takes place, as in Ni-triggered nucleation events. During Fe-triggered nucleation events, when double recalescence was observed in three instances, the apparent single nucleation events which were detected below T_0^{bcc} can be explained by the proposed model, as apparent in Figure 6-10 which compares the actual data to the model's predictions for the space and the ground-based experiments based on Equation 6.2. The model also holds when compared with the results obtained in space. The geometry in that case is different from the one described earlier for the ground-based testing. The specimen had a diameter of 7 mm and there were two independent pyrometers: the ZPY pyrometer located next to the trigger at about 1 mm and the RAD pyrometer situated at a right angle as on the ground. Figure 6-10 shows that no single events were observed in the temperature range where central nucleation is always detected suggesting that no edge nucleation occurred. There is therefore a difference in behavior since edge nucleation events were seen during ground-based testing. The central nucleation mechanism appears to be favored in micro-gravity and it is thus suspected that convection plays a role and promotes edge nucleation.

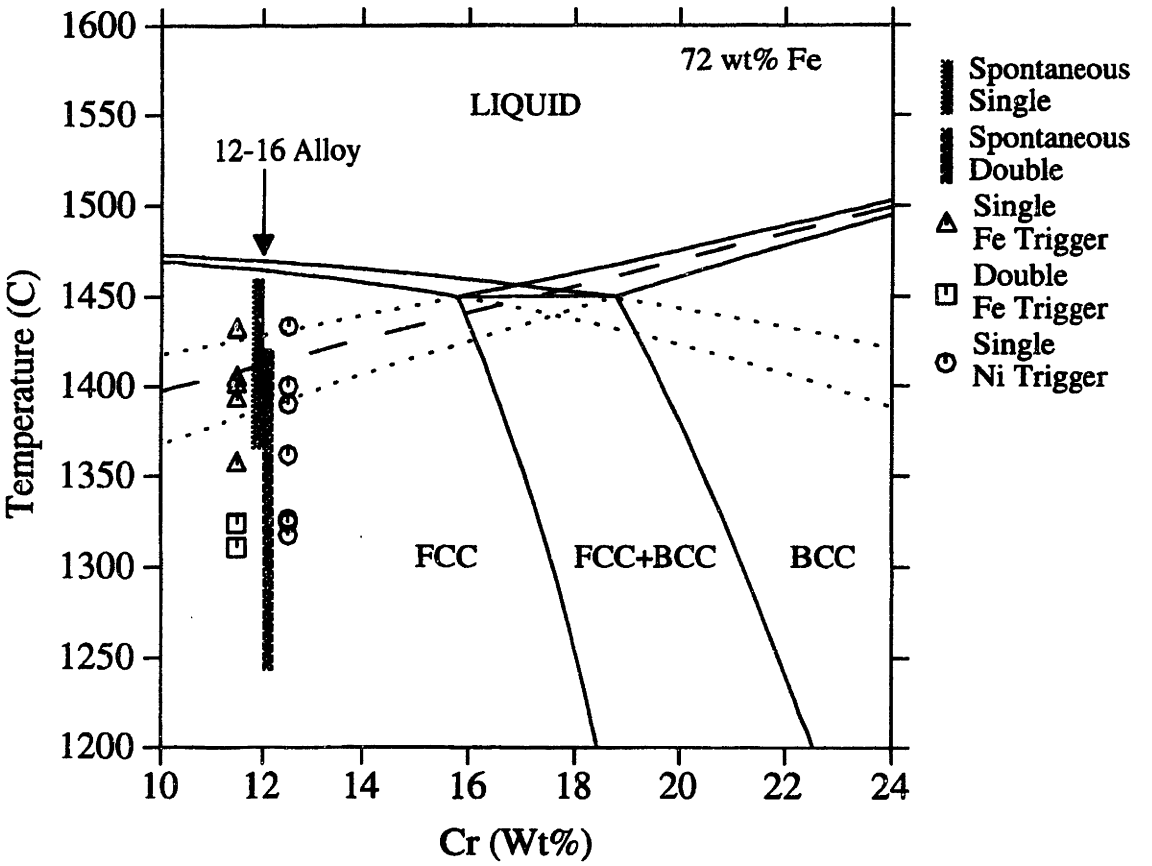

Figure 6-1: Phase selection diagram derived from the ground-based experiments.

The T_0 temperature is represented with a dashed line.

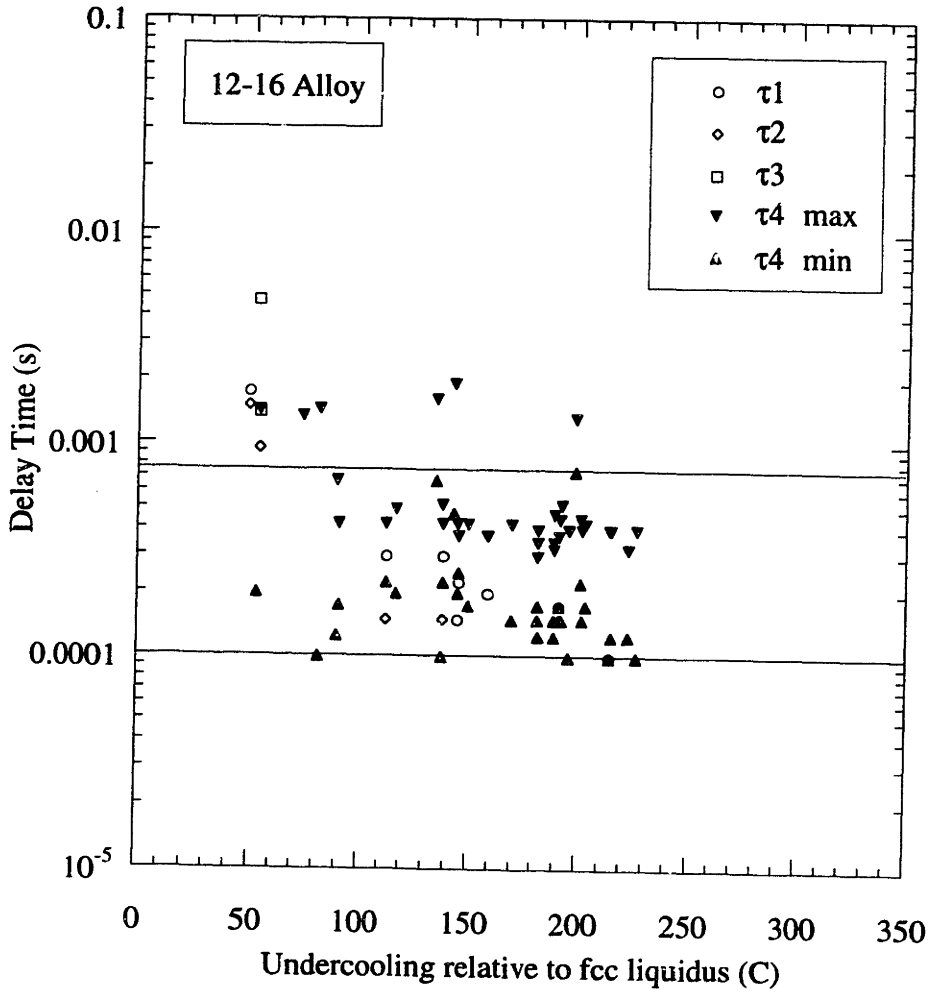

Figure 6-2: Delay time obtained using a high-speed video technique

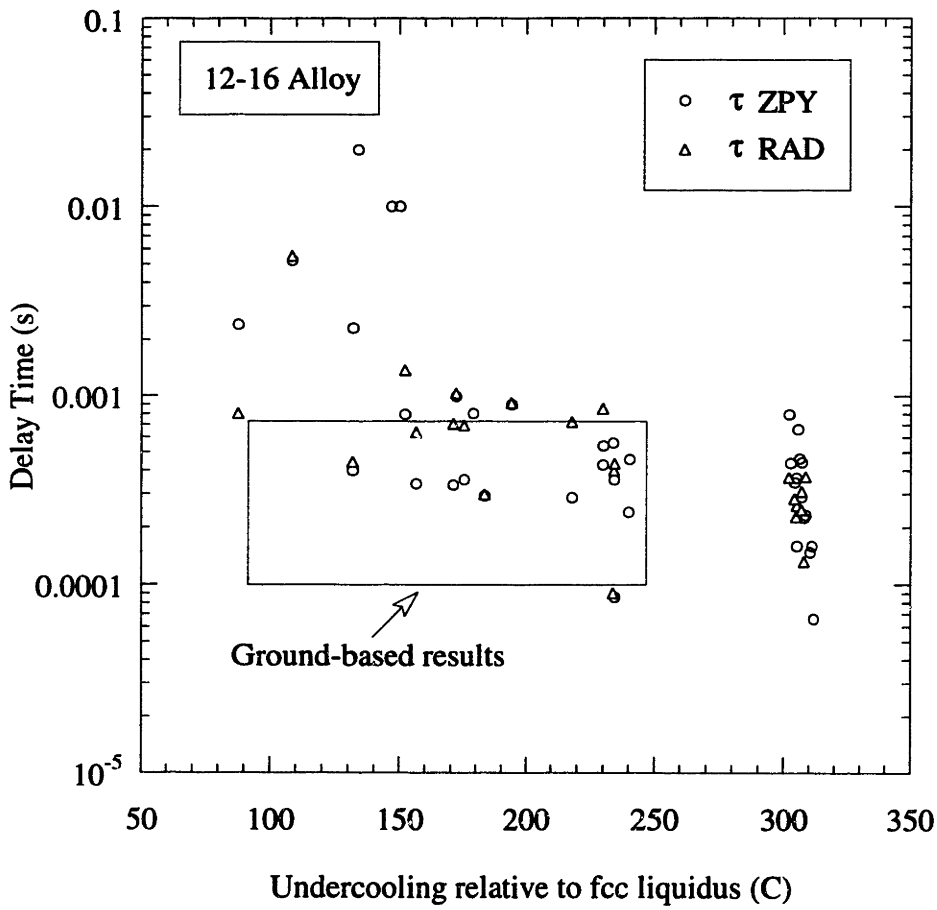

Figure 6-3: Comparison of delay times measured in space and ground-based testing

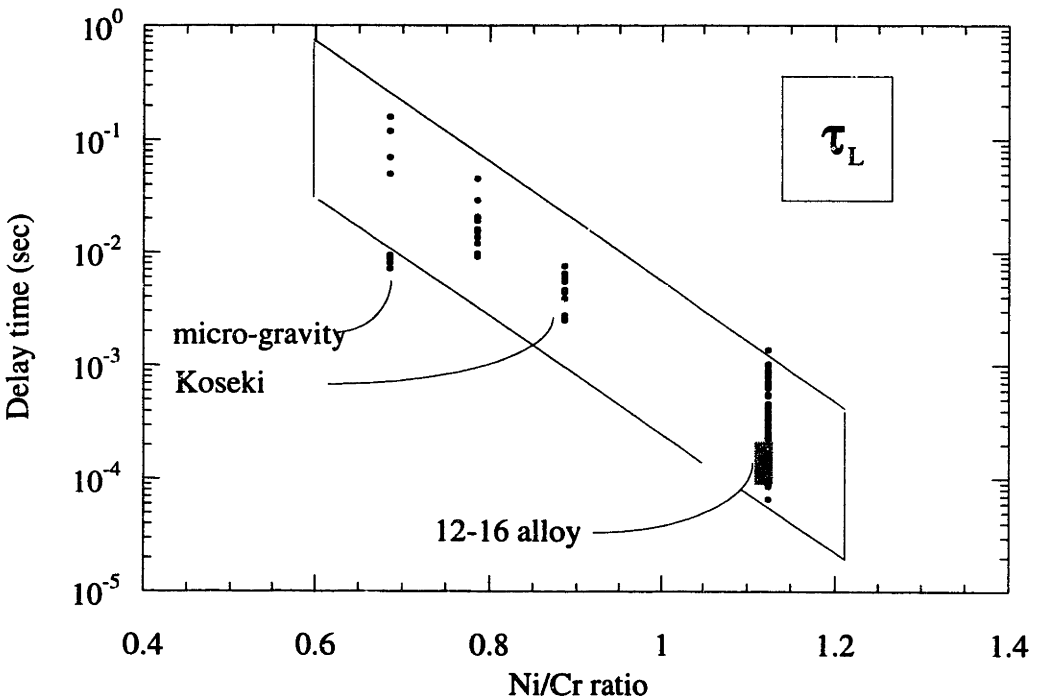

Figure 6-4: Delay time dependence on composition

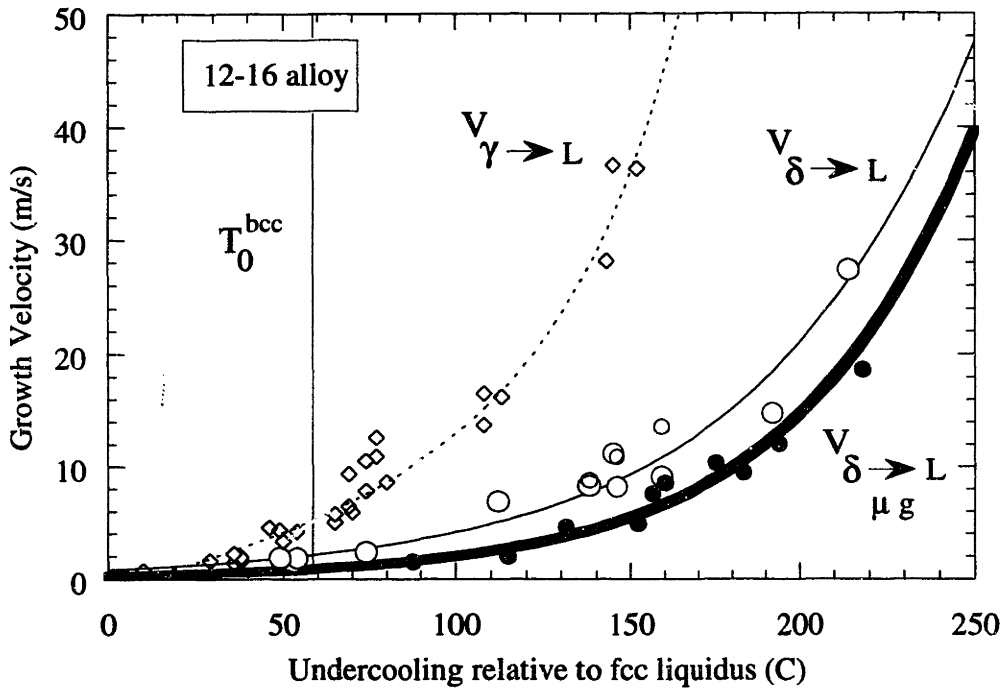

Figure 6-5: Velocity of the bcc phase from ground-based and space experiment

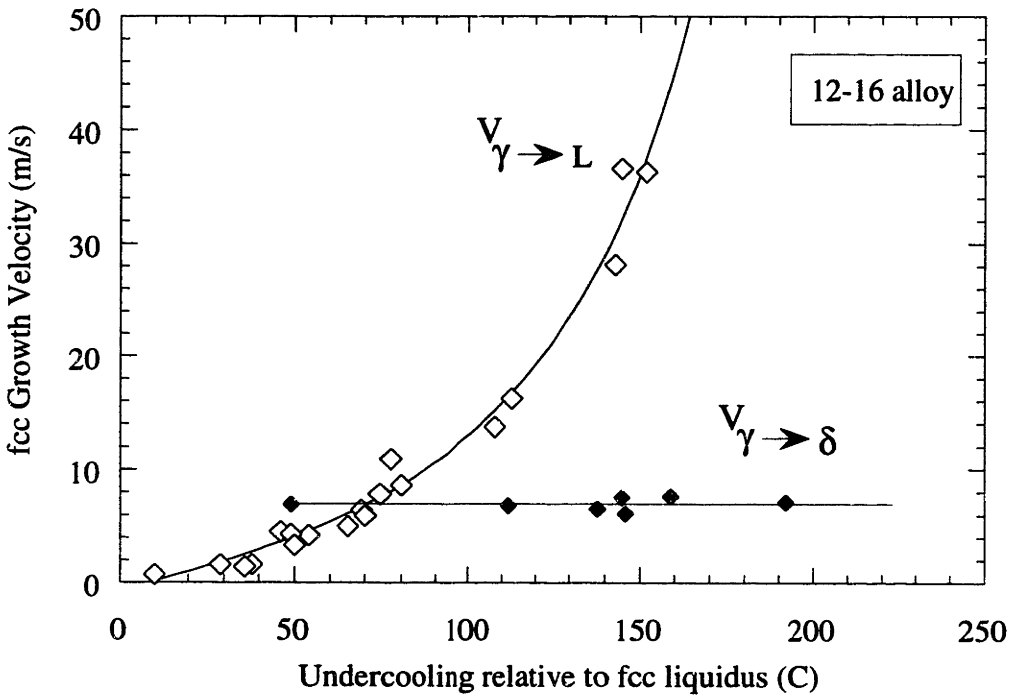

Figure 6-6: Velocity of the fcc phase

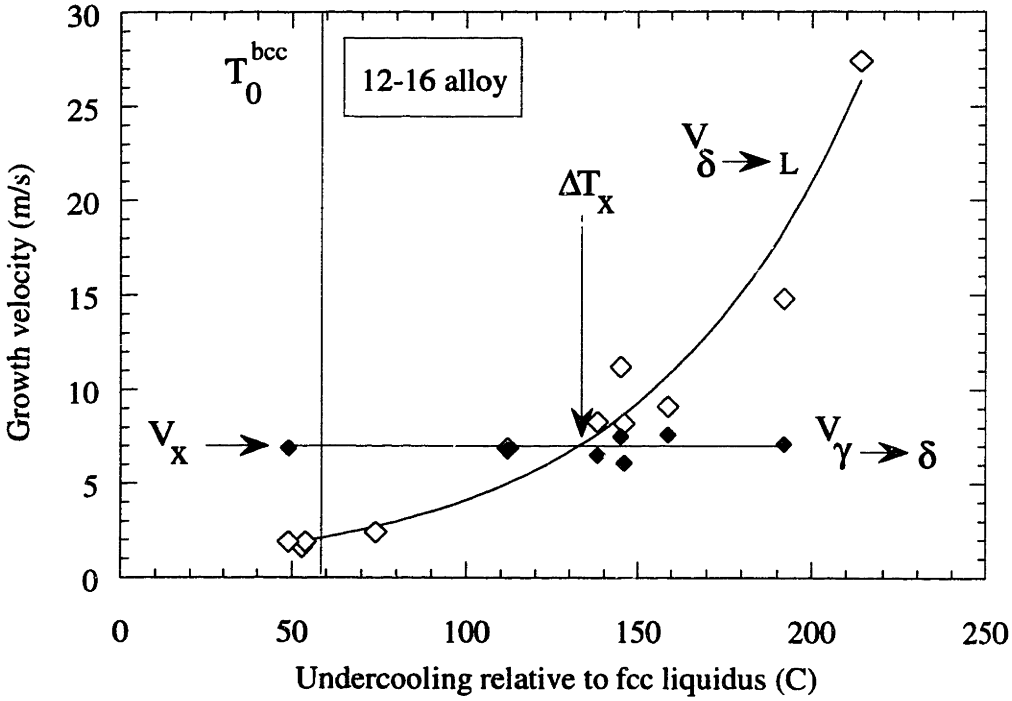

Figure 6-7: Cross-over velocity and undercooling

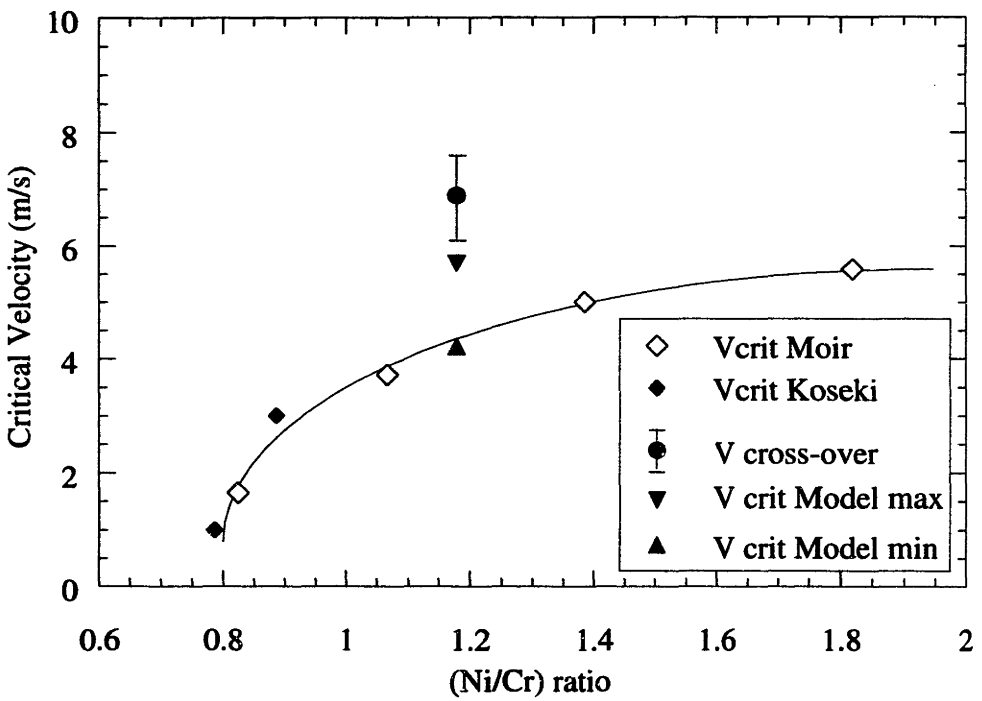

Figure 6-8: Reported critical velocities

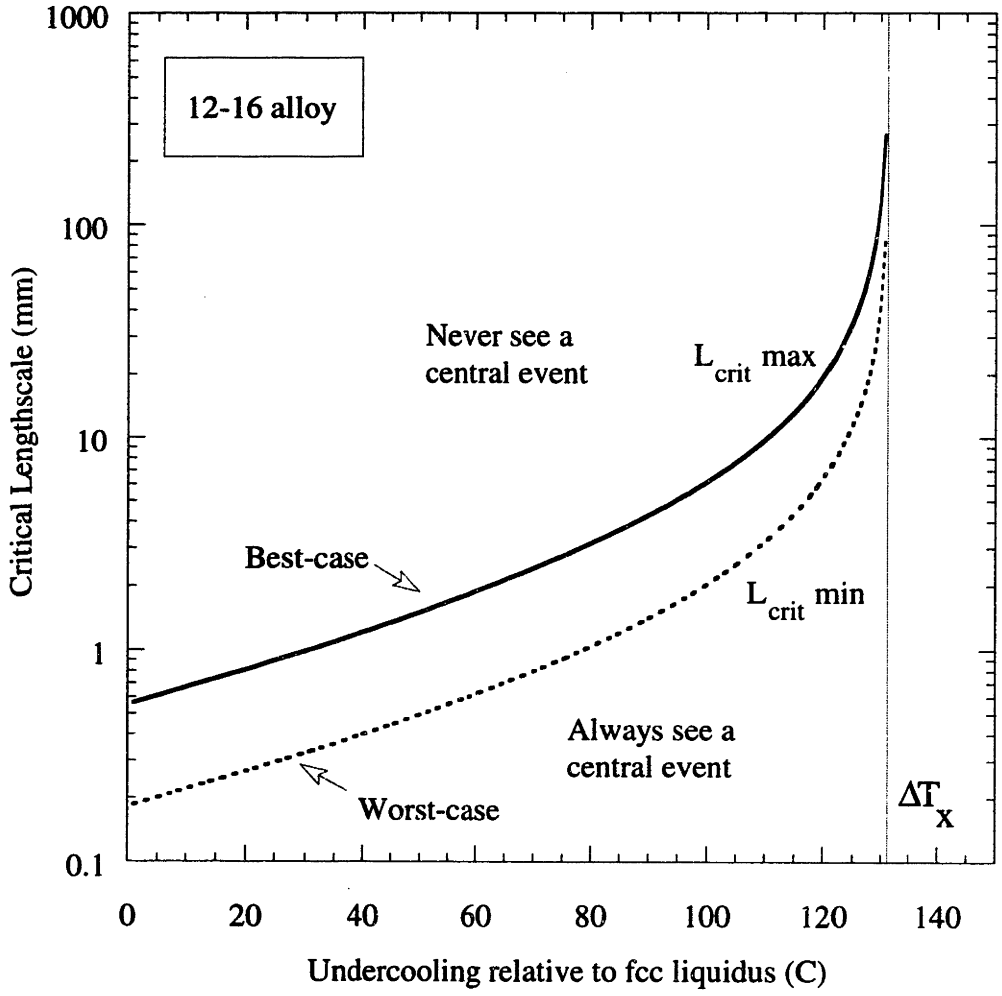

Figure 6-9: Critical lengthscale derived from Model

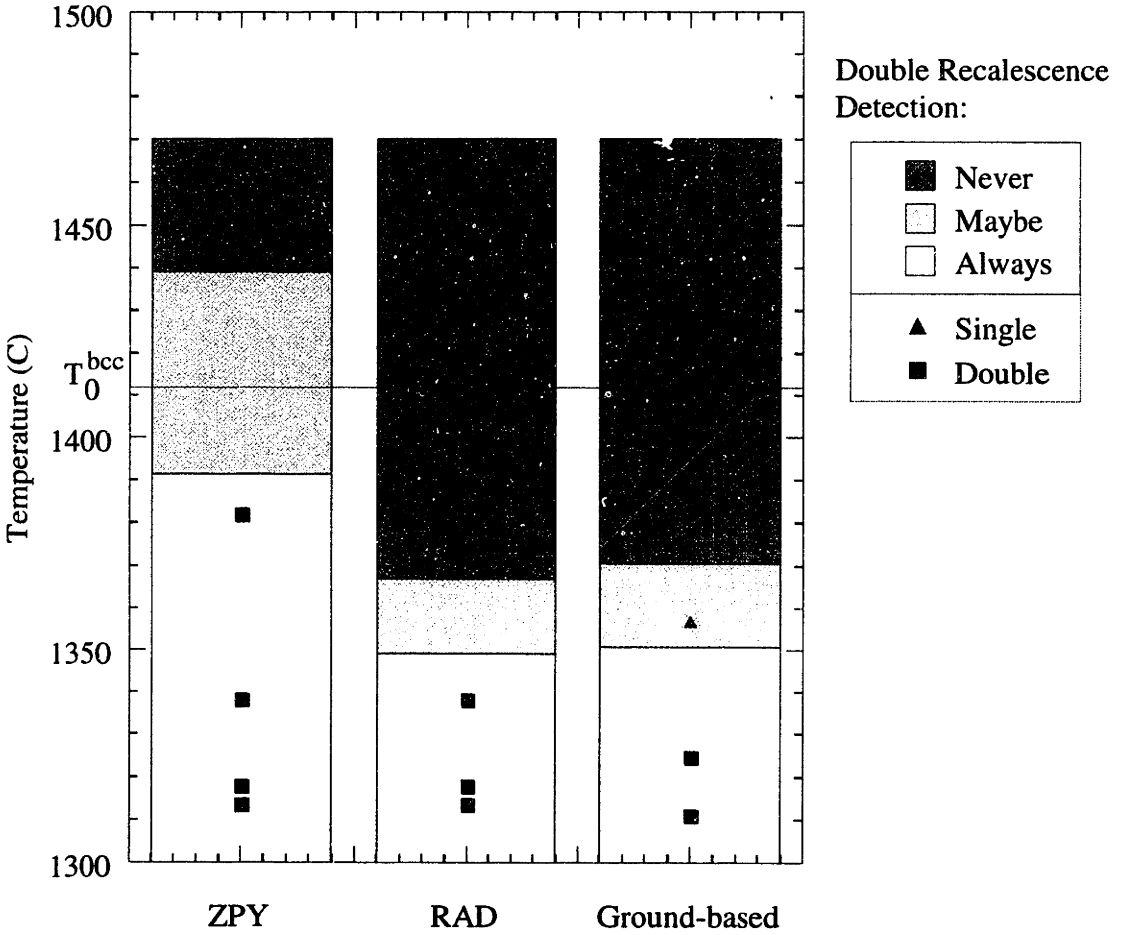

Figure 6-10: Comparison between 1-g and micro-gravity

Chapter 7

Conclusion

7.1 Phase Selection

1. Double recalescence events were observed for the first time at much lower undercoolings than previously reported defining a value of the critical transition temperature T'' for the formation of the metastable δ phase near its T_0 temperature.

2. Phase selection was successfully performed by use of different trigger materials. At temperatures below the bcc T_0, a bcc Fe trigger induced the primary nucleation of the metastable bcc phase which subsequently transformed into the stable fcc phase while an fcc Ni trigger caused the nucleation of the equilibrium fcc phase.

7.2 Delay Times

1. Delay times between the two nucleation events of a double recalescence were measured using a video technique.

2. The location of the sensor view area relative to the nucleation site was found to significantly affect the measured delay times by introducing a bias dependent on growth conditions.

3. Delay times from space and ground-based experiments for the Fe-12 wt% Cr-16 wt% Ni alloy are in good agreement. However, delay times measured in micro-gravity are slightly greater and are thus potentially influenced by convection.

7.3 Velocity

1. The velocity as a function of undercooling was characterized for growth of the δ and γ phase into the undercooled liquid using a video imaging technique.

   - It was confirmed that at all undercoolings, the growth of γ is faster than that of δ.
   - The velocities $V_{\delta \rightarrow L}$ and $V_{\gamma \rightarrow L}$ are a strong function of Fe content and a weak function of the Ni/Cr ratio.
   - Micro-gravity environment shows no significant difference in the velocity of δ, $V_{\delta \rightarrow L}$ for $\Delta T < 220$ C.

2. The growth of the stable phase into a slurry of metastable bcc and liquid resulting from primary recalescence was measured for the Fe-12 wt% Cr-16 wt% Ni alloy.

   - The velocity averaged 6.9 m/sec and was independent of the original undercooling over the range: 49 C $< \Delta T <$192 C as measured relative to the liquidus temperature of the stable phase.
   - $V_{\gamma \rightarrow \delta}$ is a strong function of the Ni/Cr ratio. It was proposed that this dependence can be related to the composition dependence of the T_0 temperatures of δ and γ.

3. Below a certain critical undercooling ΔT_X, the growth of the metastable phase into the undercooled liquid is slower than that of the equilibrium phase into the primary semi-solid:

$$V_{\delta \rightarrow L} < V_{\gamma \rightarrow \delta}$$

   The stable γ can therefore overwhelm the metastable δ and break-out into the virgin liquid. This critical undercooling is higher than that measured by previous researchers, $\Delta T_X > \Delta T_{crit}$.

7.4 Mechanism for Secondary Nucleation

1. In this work, no double recalescence was detected with high-speed pyrometry. Detection was only possible using a video technique. However, double recalescence events were observed using pyrometry during the space experiment. It is therefore hypothesized that the edge nucleation mechanism is reduced in micro-gravity.

2. A model based on both growth and delay time arguments was proposed to account for the discrepancy between this work and earlier investigations. It explains why previous studies found a higher value for the critical undercooling necessary for the nucleation of the metastable δ phase. The model also suggests that the difference in secondary nucleation mechanism between micro-gravity and ground-based experiments can be attributed to the role of convection.

Chapter 8

Suggestions for Future Work

Several directions are proposed for future research. The observed deviation from the experimental data of the LKT model needs to be investigated. The measurements of growth velocity and delay times at other composition should be carried out in order to determine their compositional dependence. The micro-gravity experiments should be continued, but as ground-based testing suggested, with the additional use of high-speed video to obtain more accurate results.

Appendix A

Pseudo-binary diagram

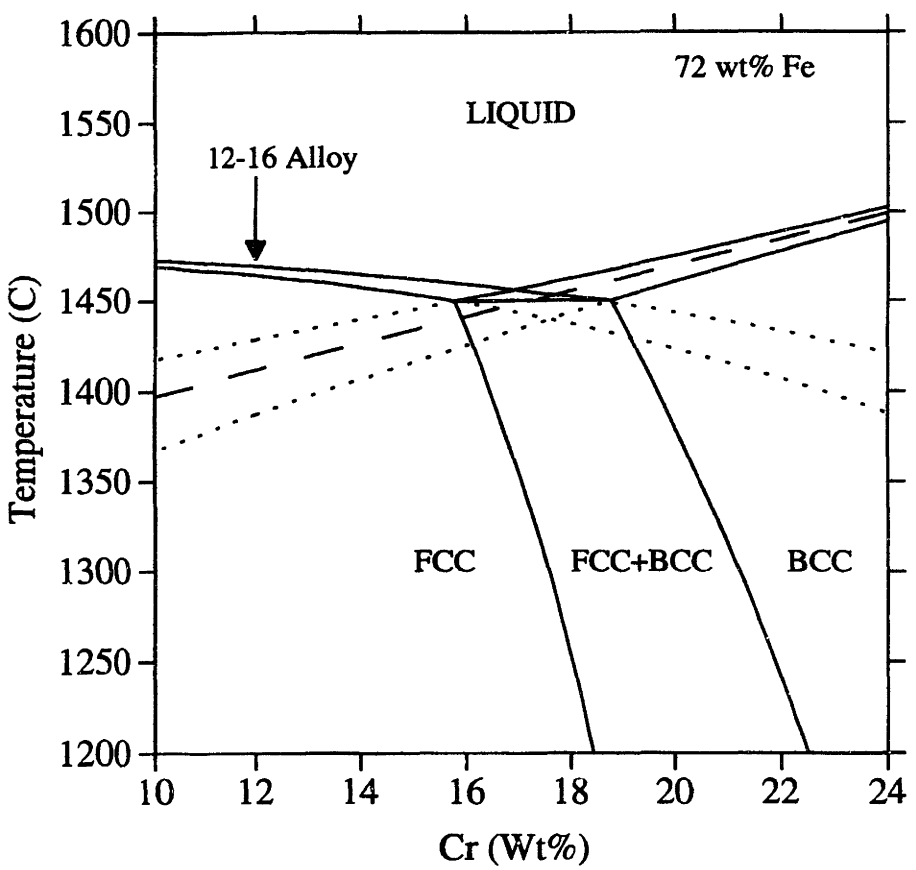

Figure A-1: Pseudo-binary diagram calculated with Thermo-Calc
The T_0 temperature is represented with a dashed line.

Appendix B

Maple Code of the LKT Model

General LKT/KBT analysis program

All thermodynamic constants will be expressed in SI units.

```
> omega := 7.71e-6;
```

Molar volume in m^3/mol

Koseki

$$\omega := .771\,10^{-5}$$

```
> C0_fcc := 12;
> C0_bcc := 16;
```

Solute concentration in wt%

$$C0\_fcc := 12$$

$$C0\_bcc := 16$$

```
> T_L_fcc := 1742.7436;
> T_L_bcc := 1701.5471;
```

Liquidus Temperature in K (all liquid)

Thermo-Calc

$$T\_L\_fcc := 1742.7436$$

$$T\_L\_bcc := 1701.5471$$

```
> T_S_fcc := 1737.615;
> T_S_bcc := 1660.5813;
```

Solidus Temperature in K (all solid)

Thermo-Calc

$$T\_S\_fcc := 1737.615$$

$$T\_S\_bcc := 1660.5813$$

```
> H_fcc := 12145.641/omega;
> H_bcc := 10803.244/omega;
```

Latent heat of fusion in J/m^3

Hm(liq,all liquid)@T_L_phi - Hm(phi,all phi)@T_S_phi

Thermo-Calc

fcc: 12145.641 J/mol

bcc: 10803.244 J/mol

$$H\_fcc := .1575310116\,10^{10}$$

$$H\_bcc := .1401198962\,10^{10}$$

```
> delS_fcc := 6.979043/omega;
> delS_bcc := 6.416997/omega;
```

Entropy of fusion in J/m^3K

Sm(liq,all liquid)@T_L_phi - Sm(phi,all phi)@T_S_phi

Thermo-Calc

fcc: 6.979043 J/molK

bcc: 6.416997 J/molK

$$delS\_fcc := 905193.6445$$

$$delS\_bcc := 832295.3306$$

```
> ke_fcc := 0.888043311;
```

Partition ratio of Cr (liq/fcc) @T_S_fcc

Thermo-Calc

$$ke\_fcc := .888043311$$

```
> ke_bcc := 0.749733811;
```

Partition ratio of Ni (liq/bcc) @T_S_bcc

Thermo-Calc

$$ke\_bcc := .749733811$$

```
> m_L_fcc := -2.8453171;
> m_L_bcc := -6.8993385;
```

Slope of liquidus in K/wt%

Assuming rejection of Cr for fcc (Fe/Ni=cte) and Ni for bcc (Fe/Cr=cte)

Thermo-Calc

$$m\_L\_fcc := -2.8453171$$

$$m\_L\_bcc := -6.8993385$$

```
> c_p := 43.8/omega;
```

Heat Capacity in J/m^3K

Koseki Mean value: 43.8 J/molK

$$c\_p := .5680933851\,10^{7}$$

```
> sigma_fcc := 0.313050813;
> sigma_bcc := 0.227100077;
```

Solid-liquid interfacial energy at T_S_phi in J/m^2

Using Spaepen-Thompson model

$$sigma\_fcc := .313050813$$

$$sigma\_bcc := .227100077$$

```
> alpha := 5.4e-6;
```

Thermal diffusivity in m^2/s

Koseki

$$\alpha := .54\,10^{-5}$$

```
> D_s_fcc := 2.67e-7*exp(-6.69e4/(8.314*T_S_fcc));
> D_s_bcc := 4.92e-7*exp(-6.77e4/(8.314*T_S_bcc));
```

Diffusivity at T_S_phi

Solute diffusivity in m^2/s for

Cr in liquid

Diffusion constant D0 = 2.67e-7 m^2/s

Activation energy Q = 6.69e4 J/mol

Ni in liquid

Diffusion constant D0 = 4.92e-7 m^2/s

Activation energy Q = 6.77e4 J/mol

Koseki

$$D\_s\_fcc := .2602257088\,10^{-8}$$

$$D\_s\_bcc := .3650410203\,10^{-8}$$

```
> sigma_star := 1/(4*Pi^2);
```

Marginal stability constant for parabolic tip

Koseki

$$sigma\_star := \frac{1}{4}\,\frac{1}{\pi^2}$$

```
> a_0 := 1e-9;
```

Atomic spacing in liquid 1e-9 m

Koseki

$$a\_0 := .1\,10^{-8}$$

```
> kl := 35;
```

Thermal conductivity of liquid in J/mKs

Koseki

$$kl := 35$$

```
> ks := 35;
```

Thermal conductivity of solid in J/mKs

k fcc = 35

k bcc = 35

Koseki

$$ks := 35$$

```
> kappa := kl/ks;
```

$$\kappa := 1$$

```
> beta_fcc := 1.4;
> beta_bcc := 1;
```

Ratio of thermal diffusivity in liquid/solid

liq/fcc: 1.4

liq/bcc: 1

Koseki

$$beta\_fcc := 1.4$$

$$beta\_bcc := 1$$

```
> Vs_fcc := 4000;
> Vs_bcc := 300;
```

Speed of sound in liquid in m/s

Koseki Vs = 2000 m/s

Iida and Guthrie value: 4036 m/s

Moir & Herlach: Vs_fcc = 4000 m/s and Vs_bcc = 300 m/s

$$Vs\_fcc := 4000$$

$$Vs\_bcc := 300$$

```
> mu_fcc := H_fcc*omega*Vs_fcc/(8.314*T_L_fcc*T_L_fcc);
> mu_bcc := H_bcc*omega*Vs_bcc/(8.314*T_L_bcc*T_L_bcc);
```

Kinetic coefficient

Koseki

$$mu\_fcc := 1.923992692$$

$$mu\_bcc := .1346410437$$

```
> k := (V, ke, D_s) -> (ke+V*a_0/D_s)/(1+V*a_0/D_s);
```

Correction for non-equilibrium effects on partition coefficient

$$k := (V,\ ke,\ D\_s) \rightarrow \frac{ke + \frac{V\ a\_0}{D\_s}}{1 + \frac{V\ a\_0}{D\_s}}$$

```
> m_v := (V, m_L, ke, D_s) ->
m_L*(1+(ke-k(V,ke,D_s)*(1-ln(k(V,ke,D_s)/ke)))/(1-ke));
```

Correction for kinetic effect on phase diagram slope

$$m\_v := (V,\ m\_L,\ ke,\ D\_s) \rightarrow m\_L \left(1 + \frac{ke - \mathrm{k}(V,\ ke,\ D\_s)\,(1 - \ln(\frac{\mathrm{k}(V,\ ke,\ D\_s)}{ke}))}{1 - ke}\right)$$

With all physical constants input, here are the equations to predict growth:

```
> J := 0;
```

Heat extraction rate in W/m^2

Assume J = 0 for LKT

$$J := 0$$

Ivantsov function (a function of a Peclet number):

```
> Iv := (P) -> P*exp(P)*Ei(1,P);
```

$$Iv := P \rightarrow P\,e^{P}\,\mathrm{Ei}(1,\ P)$$

Thermal Peclet number:

```
> P_t := (V, R) -> R*V/(2*alpha);
```

$$P\_t := (V,\ R) \rightarrow \frac{1}{2}\,\frac{R\,V}{\alpha}$$

Solutal Peclet number:

```
> P_c := (V, R, D_s) -> R*V/(2*D_s);
```

$$P\_c := (V,\ R,\ D\_s) \rightarrow \frac{1}{2}\,\frac{R\,V}{D\_s}$$

Stability parameters:

```
> zeta_L := (P_t, beta) -> ((1+kappa)*(-1+sqrt(1+1/(sigma_star*P_t*P_t))))
/(kappa*(1+sqrt(1+1/(sigma_star*P_t*P_t)))
+(-beta+sqrt(beta*beta+1/(sigma_star*P_t*P_t))));
```

$$zeta\_L := (P\_t,\ \beta) \rightarrow \frac{(1+\kappa)\,(-1+\sqrt{1+\frac{1}{sigma\_star\ P\_t^2}})}{\kappa\,(1+\sqrt{1+\frac{1}{sigma\_star\ P\_t^2}})-\beta+\sqrt{\beta^2+\frac{1}{sigma\_star\ P\_t^2}}}$$

```
> zeta_S := (P_t, beta) ->
((1+kappa)*(beta+sqrt(beta*beta+1/(sigma_star*P_t*P_t))))/(kappa*(1+sqrt(1
+1/(sigma_star*P_t*P_t)))+(-beta+sqrt(beta*beta+1/(sigma_star*P_t*P_t))));
```

$$zeta\_S := (P\_t,\ \beta) \rightarrow \frac{(1+\kappa)\,(\beta+\sqrt{\beta^2+\frac{1}{sigma\_star\ P\_t^2}})}{\kappa\,(1+\sqrt{1+\frac{1}{sigma\_star\ P\_t^2}})-\beta+\sqrt{\beta^2+\frac{1}{sigma\_star\ P\_t^2}}}$$

```
> zeta_C := (P_c, k) -> 1+2*k/(1-2*k-sqrt(1+1/(sigma_star*P_c*P_c)));
```

$$zeta\_C := (P\_c,\ k) \rightarrow 1+2\,\frac{k}{1-2\,k-\sqrt{1+\frac{1}{sigma\_star\ P\_c^2}}}$$

Constitutional undercooling:

```
> delT_c := (P_c, k, m_v, C0, m_L)-> m_v*C0*(1-(m_v/m_L)/(1-(1-k)*Iv(P_c)));
```

$$delT\_c := (P\_c,\ k,\ m\_v,\ C0,\ m\_L) \rightarrow m\_v\ C0\,(1-\frac{m\_v}{m\_L\,(1-(1-k)\,\mathrm{Iv}(P\_c))})$$

Capillary undercooling:

```
> delT_r := (R, delS, sigma) -> 2*sigma/(R*delS);
```

$$delT\_r := (R,\ delS,\ \sigma) \rightarrow 2\,\frac{\sigma}{R\ delS}$$

Kinetic undercooling:

```
> delT_k := (V, mu) -> V/mu;
```

$$delT\_k := (V,\ \mu) \rightarrow \frac{V}{\mu}$$

Ivantsov thermal undercooling solution:

```
> delT_t := (V, R, H) -> ((H-J/V)/c_p)*Iv(P_t(V,R));
```

$$delT\_t := (V,\ R,\ H) \rightarrow \frac{(H-\frac{J}{V})\,\mathrm{Iv}(\mathrm{P\_t}(V,\ R))}{c\_p}$$

```
> A := (V, R, sigma, delS) ->
sigma/(4*delS*sigma_star*alpha*alpha*P_t(V,R)*P_t(V,R));
```

$$A := (V,\ R,\ \sigma,\ delS) \rightarrow \frac{1}{4}\,\frac{\sigma}{delS\ sigma\_star\ \alpha^2\,\mathrm{P\_t}(V,\ R)^2}$$

```
> B := (V, R, H, beta, m_L, ke, D_s, C0) ->
kappa*H*zeta_L(P_t(V,R),beta)/(kl*(1+kappa))
+m_v(V,m_L,ke,D_s)*C0*(k(V,ke,D_s)-1)*zeta_C(P_c(V,R,D_s),k(V,ke,D_s))
/(D_s*(1-(1-k(V,ke,D_s))*Iv(P_c(V,R,D_s))));
```

$$B := (V,\ R,\ H,\ \beta,\ m\_L,\ ke,\ D\_s,\ C0) \rightarrow \frac{\kappa\, H\, \mathrm{zeta\_L}(\mathrm{P\_t}(V,\ R),\ \beta)}{kl\,(1+\kappa)} + \mathrm{m\_v}(V,\ m\_L,\ ke,\ D\_s)\ C0\,(\mathrm{k}(V,\ ke,\ D\_s)-1)\,\mathrm{zeta\_C}(\mathrm{P\_c}(V,\ R,\ D\_s),\ \mathrm{k}(V,\ ke,\ D\_s))/(D\_s\ (1-(1-\mathrm{k}(V,\ ke,\ D\_s))\,\mathrm{Iv}(\mathrm{P\_c}(V,\ R,\ D\_s))))$$

```
> C := (V, R, beta) ->
kappa*J*(zeta_L(P_t(V,R),beta)+zeta_S(P_t(V,R),beta))/(kl*(1+kappa));
```

$$C := (V,\ R,\ \beta) \rightarrow \frac{\kappa\, J\,(\mathrm{zeta\_L}(\mathrm{P\_t}(V,\ R),\ \beta) + \mathrm{zeta\_S}(\mathrm{P\_t}(V,\ R),\ \beta))}{kl\,(1+\kappa)}$$

Here is the actual equation defining R (here, R_th or theoretical) in terms of V and itself:

```
> R_th := (V, R, sigma, delS, beta, H, m_L, ke, D_s, C0) ->
sigma/(sigma_star*delS*R*(B(V,R,H,beta,m_L,ke,D_s,C0)*V-C(V,R,beta)));
```

$$R\_th := (V,\ R,\ \sigma,\ delS,\ \beta,\ H,\ m\_L,\ ke,\ D\_s,\ C0) \rightarrow \frac{\sigma}{sigma\_star\ delS\ R\,(\mathrm{B}(V,\ R,\ H,\ \beta,\ m\_L,\ ke,\ D\_s,\ C0)\,V - \mathrm{C}(V,\ R,\ \beta))}$$

With the equation above, we can numerically solve for R given any V value:

This section iterates through a user-defined series of velocities

10^nstart or vstart: where to begin iteration

10^nend or vend: where to stop iteration

1 or vstep: step function

Result is a series of unique solutions to the dendrite tip radii and undercooling contributions for each velocity

The output is in tab-delimited column format

*** NOTE: If the iteration refuses to converge for some conditions, you'll have to alter the search range defined for R in the "fsolve" step on line 3 of the expression below.

```
> nstart := -4; nend := -1;
```

$$nstart := -4$$

$$nend := -1$$

```
> writeto('1216.txt'); print(printf('vel\tdelT_fcc\tdelT_bcc\trad_fcc
\rad_bcc\tP_t_fcc\tP_t_bcc\tP_c_fcc\tP_c_bcc\tdelT_t_fcc\tdelT_t_bcc
\tdelT_c_fcc\tdelT_c_bcc\tdelT_r_fcc\tdelT_r_bcc\tdelT_k_fcc\tdelT_k_bcc\r'));
for nval from nstart by 1 to nend do for n from 1 by 3 to 7 do writeto(terminal);
rval_fcc := fsolve(R=subs(V=n*10^nval,R_th(V,R,sigma_fcc,delS_fcc,beta_fcc,
H_fcc,m_L_fcc,ke_fcc,D_s_fcc,C0_fcc)),R,R=1e-9..1e-4);
Pt_fcc := P_t(n*10^nval,rval_fcc); Pc_fcc := P_c(n*10^nval,rval_fcc,D_s_fcc);
```

```
delTt_fcc := evalf(subs(V=n*10^nval,R=rval_fcc,delT_t(V,R,H_fcc)));
delTc_fcc := evalf(subs(k=k(n*10^nval,ke_fcc,D_s_fcc),(subs(V=n*10^nval,
R=rval_fcc,delT_c(P_c(V,R,D_s_fcc),k(V,ke_fcc,D_s_fcc),m_v(V,m_L_fcc,ke_fcc,
D_s_fcc),C0_fcc,m_L_fcc))))); delTr_fcc := delT_r(rval_fcc,delS_fcc,sigma_fcc);
delTk_fcc := delT_k(n*10^nval,mu_fcc);
delT_fcc := delTt_fcc+delTc_fcc+delTr_fcc+delTk_fcc;
rval_bcc := fsolve(R=subs(V=n*10^nval,R_th(V,R,sigma_bcc,delS_bcc,beta_bcc,
H_bcc,m_L_bcc,ke_bcc,D_s_bcc,C0_bcc)),R,R=1e-9..1e-4);
Pt_bcc := P_t(n*10^nval,rval_bcc); Pc_bcc := P_c(n*10^nval,rval_bcc,D_s_bcc);
delTt_bcc := evalf(subs(V=n*10^nval,R=rval_bcc,delT_t(V,R,H_bcc)));
delTc_bcc := evalf(subs(k=k(n*10^nval,ke_bcc,D_s_bcc),(subs(V=n*10^nval,
R=rval_bcc,delT_c(P_c(V,R,D_s_bcc),k(V,ke_bcc,D_s_bcc),m_v(V,m_L_bcc,ke_bcc,
D_s_bcc),C0_bcc,m_L_bcc))))); delTr_bcc := delT_r(rval_bcc,delS_bcc,sigma_bcc);
delTk_bcc := delT_k(n*10^nval,mu_bcc);
delT_bcc := delTt_bcc+delTc_bcc+delTr_bcc+delTk_bcc; appendto('1216.txt');
print(printf('%e\t%e\t%e\t%e\t%e\t%e\t%e\t%e\t%e\t%e\t%e\t%e\t%e\t%e\t%e\t%e\t%e\t%e\t%e\t
%e\r',n*10^nval,delT_fcc,delT_bcc,rval_fcc,rval_bcc,Pt_fcc,Pt_bcc,Pc_fcc,
Pc_bcc,delTt_fcc,delTt_bcc,delTc_fcc,delTc_bcc,delTr_fcc,delTr_bcc,delTk_fcc,
delTk_bcc)); od; od; writeto(terminal);
```

```
> vstart := 1; vend := 30; vstep := 1;
```

$$vstart := 1$$

$$vend := 30$$

$$vstep := 1$$

```
> for vval from vstart by vstep to vend do writeto(terminal); rval_fcc :=
fsolve(R=subs(V=vval,R_th(V,R,sigma_fcc,delS_fcc,beta_fcc,H_fcc,m_L_fcc,ke_fcc,
D_s_fcc,C0_fcc)),R,R=1e-9..1e-4); Pt_fcc := P_t(vval,rval_fcc);
Pc_fcc := P_c(vval,rval_fcc,D_s_fcc); delTt_fcc := evalf(subs(V=vval,R=rval_fcc,
delT_t(V,R,H_fcc))); delTc_fcc := evalf(subs(k=k(vval,ke_fcc,D_s_fcc),
(subs(V=vval,R=rval_fcc,delT_c(P_c(V,R,D_s_fcc),k(V,ke_fcc,D_s_fcc),
m_v(V,m_L_fcc,ke_fcc,D_s_fcc),C0_fcc,m_L_fcc))))); delTr_fcc := delT_r(rval_fcc,
delS_fcc,sigma_fcc); delTk_fcc := delT_k(vval,mu_fcc);
delT_fcc := delTt_fcc+delTc_fcc+delTr_fcc+delTk_fcc;
rval_bcc := fsolve(R=subs(V=vval,R_th(V,R,sigma_bcc,delS_bcc,beta_bcc,H_bcc,
m_L_bcc,ke_bcc,D_s_bcc,C0_bcc)),R,R=1e-9..1e-4); Pt_bcc := P_t(vval,rval_bcc);
Pc_bcc := P_c(vval,rval_bcc,D_s_bcc); delTt_bcc := evalf(subs(V=vval,R=rval_bcc,
delT_t(V,R,H_bcc))); delTc_bcc := evalf(subs(k=k(vval,ke_bcc,D_s_bcc),
(subs(V=vval,R=rval_bcc,delT_c(P_c(V,R,D_s_bcc),k(V,ke_bcc,D_s_bcc),
m_v(V,m_L_bcc,ke_bcc,D_s_bcc),C0_bcc,m_L_bcc))))); delTr_bcc := delT_r(rval_bcc,
delS_bcc,sigma_bcc); delTk_bcc := delT_k(vval,mu_bcc);
delT_bcc := delTt_bcc+delTc_bcc+delTr_bcc+delTk_bcc; appendto('1216.txt');
print(printf('%e\t%e\t%e\t%e\t%e\t%e\t%e\t%e\t%e\t%e\t%e\t%e\t%e\t%e\t%e\t%e\t%e\t%e\t%e\t%e
```

```
\t%e\t%e\r',vval,delT_fcc,delT_bcc,rval_fcc,rval_bcc,Pt_fcc,Pt_bcc,Pc_fcc,
Pc_bcc,delTt_fcc,delTt_bcc,delTc_fcc,delTc_bcc,delTr_fcc,delTr_bcc,delTk_fcc,
delTk_bcc)); od; writeto(terminal);
```

Appendix C

Experimental Data Fit

The experimental velocity data for the growth of δ and γ was fitted with the following equations:

- bcc

$$V_{\delta \to L} = m_0 * exp(m_1 * \Delta T)$$

where: $m_0 = 0.80691$

$m_1 = 0.016295$

- fcc

$$V_{\gamma \to L} = m_0 + m_1 * \Delta T + m_2 * \Delta T^{2.5} + exp(m_3 * \Delta T + m_4)$$

where: $m_0 = -0.73463$

$m_1 = 0.07558$

$m_2 = 3.67 * 10^{-5}$

$m_3 = 0.036486$

$m_4 = -2.7525$

Bibliography

[1] T. Koseki. *Undercooling and Rapid Solidification of Fe-Cr-Ni Ternary Alloys.* PhD thesis, Massachusetts Institute of Technology, Cambridge, MA, 1994.

[2] T. Koseki and M. C. Flemings. Solidification of undercooled Fe-Ni-Cr alloys: Part I. Thermal behavior. *Metall. Mater. Trans. A*, 26A(11):2991–2999, November 1995.

[3] T. Koseki and M. C. Flemings. Solidification of undercooled Fe-Ni-Cr alloys: Part II. Microstructural evolution. *Metall. Mater. Trans. A*, 27A(10):3226–3240, October 1996.

[4] T. Koseki and M. C. Flemings. Solidification of undercooled Fe-Ni-Cr alloys: Part III. Phase selection in chill casting. *Metall. Mater. Trans. A*, 28A(11):2385–2395, November 1997.

[5] T. Volkmann, W. Löser, and D. M. Herlach. Nucleation and phase selection in undercooled Fe-Ni-Cr melts: Part I. Theoretical analysis of nucleation behavior. *Metall. Mater. Trans. A*, 28A(2):453–460, February 1997.

[6] T. Volkmann, W. Löser, and D. M. Herlach. Nucleation and phase selection in undercooled Fe-Ni-Cr melts: Part II. Containerless solidification experiments. *Metall. Mater. Trans. A*, 28A(2):461–469, February 1997.

[7] S. A. Moir and D. M. Herlach. Observation of phase selection from dendrite growth in undercooled Fe-Ni-Cr melts. *Acta mater.*, 45(7):2827–2837, July 1997.

[8] M. C. Flemings and D. M. Matson. Alloy undercooling experiments in a microgravity environment. In F. Szofran, D. McCauley, and C. Walker, editors, *NASA Conference Publication 3342*, pages 211–216, Huntsville, Al, October 1996. NASA, MSFC.

[9] D. M. Matson. Alloy undercooling experiments, delay times and critical undercooling. In K. Samwer and I. Egry, editors, *Internationaler Workshop on Nucleation and Thermophysical Properties of Undercooled Melts*, pages 79–98, Physikzentrum Bad Honnef, Germany, March 1998.

[10] D. M. Matson, A. Shokuhfar, J. W. Lum, and M. C. Flemings. Imaging the double-recalescence behaviour of undercooled Fe-Cr-Ni alloys using a high-speed video technique. In I. Ohnaka and D. M. Stefanescu, editors, *Proc. Int. Symp. on Advanced Materials and Technology*, 117th JIM Conf., pages 19–26, Honolulu, HI, December 1995. TMS; Warrendale, PA, USA.

[11] J. W. Lum. High-speed imaging and analysis of the solidification of undercooled alloy melts. Master's thesis, Massachusetts Institute of Technology, Cambridge, MA, 1996.

[12] T. Koseki and M. C. Flemings. Effect of external heat extraction on dendritic growth into undercooled melts. *Iron Steel Inst. Jpn. Int.*, 35(6):611–617, 1995.

[13] C. V. Thompson and F. Spaepen. Homogeneous crystal nucleation in binary metallic melts. *Acta metall.*, 31(12):2021–2027, December 1983.

Biographical Note

The author was born in France and attended highschool at Lycée Marie Curie in Sceaux. He graduated with high honors in 1992 and enrolled in the preparatory classes for engineering schools at Lycée Louis le Grand in Paris. In 1994, he was admitted to École Centrale Paris where he completed the two first years of the curriculum before leaving for MIT in 1996 within a study-abroad program offered by the school.

THESIS PROCESSING SLIP

FIXED FIELD: ill. _____ name _____

index _____ biblio _____

▶ COPIES: Archives Aero Dewey Eng Hum

Lindgren Music Rotch Science

TITLE VARIES: ▶☐ _____

NAME VARIES: ▶☐ _____

IMPRINT: (COPYRIGHT) _____

▶ COLLATION: 76 l.

▶ ADD. DEGREE: _____ ▶ DEPT.: _____

SUPERVISORS: _____

NOTES:

cat'r: date:

page: 0135

▶ DEPT: MatSci&E

▶ YEAR: 1998 ▶ DEGREE: ~~M.S.~~ S.M.

▶ NAME: BUI, Quoc Cuong